Environmental Satellite Processing Center

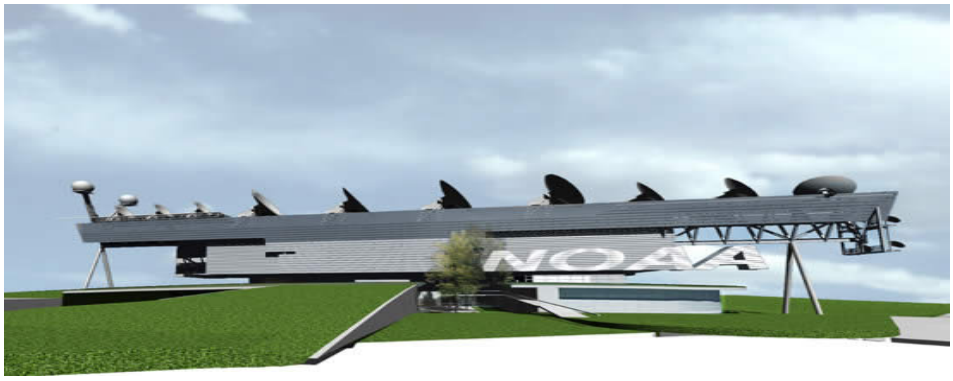

NDE Vegetation Products System (NVPS)

Green Vegetation Fraction (GVF) NOAA-Unique Product

ALGORITHM THEORETICAL BASIS DOCUMENT

Version 4.0

TITLE: GVF ALGORITHM THEORETICAL BASIS DOCUMENT

VERSION 4.0

AUTHORS:
Hanjun Ding (OSPO)
Yufeng Zhu (MAXIMUS)

APPROVAL SIGNATURES:

June 1, 2018

Hanjun Ding — Date
NVPS Product Area Lead

GVF ALGORITHM THEORETICAL BASIS DOCUMENT
VERSION HISTORY SUMMARY

Version	Description	Revised Sections	Date
1.0	New document adapted from SPSRB guidelines for GVF Critical Design Review (CDR)	New Document	03/29/2012
1.1	Revision to respond to CDR Reviewer comments	3	04/27/2012
1.2	Revision to adopt user's new request to generate daily rolling weekly GVF product	2.1, 3	6/18/2012
1.3	The affiliation for Zhangyan Jiang and Junchang Ju is changed		
2.0	Added alternative EVI2 for EVI calculation; Added description of a GVF climatology and gap filling at high latitude region in winter; Added Sensor noise characterization.	3.2, 3.3, 3.5	8/20/2013
2.1	Updated the sample results of the VIIRS GVF maps and time series; Added the GVF validation section	3.7, 3.8	9/16/2014
3.0	Updated EVI smoothing algorithm; updated GVF validation for the NVPS Algorithm Readiness Review	3.8.2, 3.8.3	11/20/2017

VERSION 1.1 CHANGES

Section	Page	Revision
3.3.6	27	Cloudy pixels are excluded from aggregation. An aggregate with all cloudy pixels is aggregated and tagged with a QC flag.
3.5.1	29	Test case analysis using unsmoothed vegetation indices is a reliable indicator that GVF retrieval using smoothed TOC EVI is the best approach.
4.1	35	Latency is not an algorithm assumption

VERSION 1.2 CHANGES

Section	Page	Revision

2.1	13	Weekly products are updated to daily rolling weekly products
2.1	14	1-km regional GVF product is added as a new requirement
3.1	15	Processing outline is updated for producing daily rolling weekly GVF products

VERSION 1.3 CHANGES

Section	Page	Revision
	2	The affiliation for Zhangyan Jiang and Junchang Ju is changed from IMSG to AER.

VERSION 2.0 CHANGES

Section	Page	Revision
3.2.4	20	The VIIRS maximum and minimum EVI values are updated.
3.3.3	29	Abnormal EVI values are replaced by alternative EVI2 values.
3.3.6	30	A GVF climatology is created and GVF gaps at high latitude region in winter are filled by the GVF climatology.
3.5.2	35	Sensor Radiometric Performance is added.
3.5.3	36	Sensor Radiometric Calibration is added.
3.5.4	37	Sensor noise Characterization is added.

VERSION 2.1 CHANGES

Section	Page	Revision
3.7	40-44	The VIIRS GVF sample maps and time series are updated
3.8	44-47	The whole GVF validation section is added

VERSION 3.0 CHANGES

Section	Page	Revision
3.3.4	31-32	The EVI time series smoothing algorithm is updated
3.8.1	44-47	Validation using Landsat data derived GVF is updated
3.8.2	47-51	Validation using GVF derived from Google Earth images is added
3.8.3	51-56	Validation of GVF seasonal variation using PhenoCam data is added

VERSION 4.0 CHANGES

Version	Description	Revised Sections	Date
4.0	Updated to version 4.0		6/1/2018

TABLE OF CONTENTS

Page

LIST OF FIGURES

Page

LIST OF TABLES

LIST OF ACRONYMS

AER	Atmospheric and Environmental Research
ARVI	Atmospheric Resistant Vegetation Index
ATBD	Algorithm Theoretical Basis Document
CDR	Critical Design Review
DoD	Department of Defense
EVI	Enhanced Vegetation Index
GVF	Green Vegetation Fraction
GVFP	Green Vegetation Fraction Product
GVPS	Global Vegetation Processing System
HDF	Hierarchical Data Format
IMSG	I. M. Systems Group
IP	Intermediate Product
LAI	Leaf Area Index
NIR	Near Infrared
km	kilometer
MB	Mega Byte
μm	micron
MODIS	Moderate Resolution Imaging Spectroradiometer
MVC	Maximum Value Compositing
NASA	National Aeronautics and Space Administration
NCEP	National Center for Environmental Prediction
NDVI	Normalized Difference Vegetation Index
NESDIS	National Environmental Satellite, Data, and Information Service
NetCDF	Network Common Data Form
NIR	Near Infrared
NOAA	National Oceanic and Atmospheric Administration
OSPO	Office of Satellite and Product Operations
PDR	Preliminary Design Review
PNG	Portable Network Graphics
QA	Quality Assurance
RIP	Retained Intermediate Product
SAVI	Soil Adjusted Vegetation Index
SEVIRI	Spinning Enhanced Visible and Infrared Imager
SNPP	Suomi National Polar-orbiting Partnership
SPSRB	Satellite Products and Services Review Board

STAR	Center for Satellite Applications and Research
TIFF	Tagged Image File Format
TOA	Top of Atmosphere
TOC	Top of Canopy
USGS	United States Geological Survey
VHP	Vegetation Health Product
VIIRS	Visible Infrared Imager Radiometer Suite

ABSTRACT

This document is the Algorithm Theoretical Basis Document (ATBD) for the Green Vegetation Fraction (GVF) operational product system, developed by the NOAA/NESDIS Center for Satellite Applications and Research (STAR). The main function of the GVF system is to produce GVF as a NOAA-Unique Product (NUP) from data from the Visible Infrared Imager Radiometer Suite (VIIRS) sensor onboard Suomi National Polar-orbiting Partnership (SNPP) satellite, for applications in numerical weather and seasonal climate prediction models at the National Centers for Environmental Prediction (NCEP). The retrieval algorithm uses VIIRS red (I1), near-infrared (I2) and blue (M3) bands centered at 0.640 μm, 0.865 μm and 0.490 μm, respectively, to calculate the Enhanced Vegetation Index (EVI) and derive GVF from EVI. This document describes the details of the GVF algorithm that is used for VIIRS GVF retrieval. To meet the data needs of NCEP and other potential users, GVF is produced as a daily rolling weekly composite at 4-km resolution (global scale) and 1-km resolution (regional scale). Details of these products are presented in Sections 2 and 3 of this document.

1. INTRODUCTION

Green Vegetation Fraction (GVF) data are needed for land surface initialization in numerical weather prediction models and land surface monitoring. The current GVF operational product is based on Top of the Atmosphere (TOA) Normalized Vegetation Index (NDVI) derived from the AVHRR sensor (NOAA-19). With the launch of the newest Earth-observing satellite, Suomi NPP (SNPP), the Visible Infrared Imager Radiometer Suite (VIIRS) onboard SNPP acquired its first measurements on November. 21, 2011. Since the SNPP era, NESDIS has sustained the production of a new real-time weekly GVF product from VIIRS. The VIIRS GVF is based on the Top of Canopy (TOC) Enhanced Vegetation Index (EVI).

The algorithm was developed by scientists and developers of STAR GVF team led by Dr. Marco Vargas, Ivan Csiszar and Yunyue Yu. The Office of Satellite and Product Operations (OSPO) will be responsible for data storage, accessibility and dissemination.

1.1 Purpose of This Document

The purpose of this document is to describe the GVF processing (GVF) algorithm in detail.

1.2 Who Should Use This Document

The intended users of this document include customers, GVF data users and GVF system operators.

1.3 Inside Each Section

This document contains the following sections:

Section 1.0 - Introduction. Section 1 provides the purpose and intended users of the ATBD.

Section 2.0 - GVF System Overview. Section 2 describes the products generated by the algorithm and the characteristics of the instruments that supply inputs to the algorithm.

Section 3.0 - Algorithm Description. Section 3 describes the algorithm, including a processing overview, input data, physical description, mathematical description, algorithm output, performance estimates, practical considerations, and validation.

Section 4.0 - Assumptions and Limitations. Section 4 states assumptions that were made in determining that the software system architecture as designed will meet the requirements, and states limitations that may impact on the system's ability to meet requirements.

Section 5.0 - List of References. Section 5 provides a list of references cited in the document.

2. GVF OVERVIEW

2.1 Objectives of Green Vegetation Fraction Retrievals

The current NOAA-AVHRR Global Vegetation Processing System (GVPS) operationally produces weekly GVF data from AVHRR at 16 km resolution for use by NCEP/EMC. Currently, GVF data are produced from NOAA-19 AVHRR. There is a need for preparation for the transition to the VIIRS instrument and ensure continuous provision of GVF data, taking also advantage of the improved VIIRS characteristics compared to AVHRR.

The NCEP requirements clearly state that "NESDIS must sustain production of this real-time weekly product from future polar-orbiting satellites, especially including NPOESS (at current or better spatial and temporal resolution)" and "The resolution of the Green Vegetation Fraction data needs to keep pace with the NWP/land model development. The North American Mesoscale model is currently being tested at 4 km resolution and will be operational in the coming years."

The GVF system is to meet the user request from NOAA-NCEP/EMC, numbered as #0812-009 in the NESDIS Satellite Products and Services Review Board (SPSRB) Request Tracking System, which requests a gridded daily rolling weekly GVF product at 4 km horizontal resolution (global scale) and a gridded daily rolling weekly GVF product at 1 km horizontal resolution (regional scale) in Lat/Lon projection.

- Gridded daily rolling weekly GVF products at 4 km horizontal resolution and in Lat/Lon projection. Specifications of the GVF data product stated by NCEP in its User Request are the following:
  1) Has a global coverage once a day;
  2) Represents the fractional area of the grid cell covered by live (green) vegetation;
  3) Has a spatial horizontal resolution of 4km;
  4) Has an accuracy of 12%;
  5) Has a measurement range from 0-100%;
  6) Has a data latency of 1 day immediately after the 7-day compositing period, updated daily
  7) Data are stored for geographic grids and data files are in GRIB2 format;
  8) Has continuity and consistency with AVHRR-based GVF data record.

- Gridded daily rolling weekly regional GVF products at 1 km horizontal resolution and in Lat/Lon projection, covering latitude 7.5° S to 90° N, longitude 130° E eastward to 30° E. Specifications of the GVF data product stated by NCEP in its User Request are the following:

  1) Has a regional coverage once a day;
  2) Represents the fractional area of the grid cell covered by live (green) vegetation;
  3) Has a spatial horizontal resolution of 1km;
  4) Has an accuracy of 12%;
  5) Has a measurement range from 0-100%;
  6) Has a data latency of 1 day immediately after the 7-day compositing period, updated daily

2.2 Instrument Characteristics

VIIRS is one of five instruments onboard the SNPP satellite that launched on Oct. 28, 2011. It is intended to be the product of a convergence between the Department of Defense (DoD), NOAA and the National Aeronautics and Space Administration (NASA) in the form of a single visible/infrared sensor capable of satisfying the needs of all three communities, as well as the research community beyond. As such, VIIRS will require three key attributes: high spatial resolution with controlled growth off nadir; minimal production and operational cost; and a sufficient number of spectral bands to satisfy the requirements for generating accurate operational and scientific products. Calibration is performed onboard using a solar diffuser for short wavelengths and a blackbody source and deep space view for thermal wavelengths. The nominal altitude for the SNPP satellite is 824 km. The VIIRS scan will therefore extend to 56 degrees on either side of nadir.

The positioning of the VIIRS Visible/Near Infrared (VNIR) and Short Wave Infrared (SWIR) spectral bands is summarized in table 1. There are nine moderate (M) resolution bands and three imagery (I) resolution bands in the VNIR and SWIR spectral region. The nadir resolutions for the M and I bands are 750 m and 375 m, respectively. The GVF algorithm uses the VIIRS bands I1, I2 and M3 as input data.

Table 1. Summary of VIIRS VNIR and SWIR Spectral Band Characteristics

Band Name	Center	Width* (microns)	Resolution (m)
M1	0.415	0.020	750
M2	0.445	0.020	750
M3	**0.490**	**0.020**	**750**
M4	0.555	0.020	750
I1	**0.640**	**0.075**	**375**
M5	0.673	0.021	750
I2	**0.865**	**0.039**	**375**
M7	0.865	0.039	750
M8	1.240	0.020	750
I3	1.610	0.060	375
M10	1.610	0.060	750
M11	2.250	0.050	750

*Full width half maximum (FWHM)

2.3 Retrieval Strategy

The basic retrieval strategy of the GVF system is to produce green vegetation fraction from VIIRS observations. Daily VIIRS surface reflectance data are composited weekly and EVI is calculated based on the composited data. EVI time series are smoothed by a smoothing algorithm. GVF is then calculated by comparison of weekly EVI to the global maximum and minimum EVI values.

3. ALGORITHM DESCRIPTION

3.1 Processing Outline

The GVF system generates daily rolling weekly Green Vegetation Fraction through the following steps:

Step 1: VIIRS swath surface reflectance data in bands I1, I2, and M3 during a calendar day (0000 – 2400 UTC) are mapped to the native GVF geographic grid (0.003 degree plate carrée projection) to produce a gridded daily surface reflectance map.

Step 2: At the end of a 7-day period, the daily surface reflectance maps of the 7 days are composited to produce a weekly surface reflectance map using the MVA-SAVI compositing algorithm, which selects, at each GVF grid point (pixel), the observation with maximum view-angle adjusted SAVI value in the 7-day period. The 7-day compositing is conducted daily using data in the previous 7 days as input data, which is called daily rolling weekly compositing. Cloud mask information of composited pixels is saved.

Step 3: EVI is calculated from the daily rolling weekly composited VIIRS surface reflectance data in bands I1, I2 and M3.

Step 4: High frequency noise in EVI is reduced by applying a 15-week digital smoothing filter on EVI.

Step 5: GVF is calculated by comparing the smoothed EVI against the global maximum and minimum EVI values assuming a linear relationship between EVI and GVF.

Step 6: GVF is aggregated to 0.009 degree and 0.036 degree resolutions for output maps. Potential gaps on the output maps at high latitudes are filled using monthly VIIRS GVF climatology.

The algorithm processing flow is shown in Figure 1.

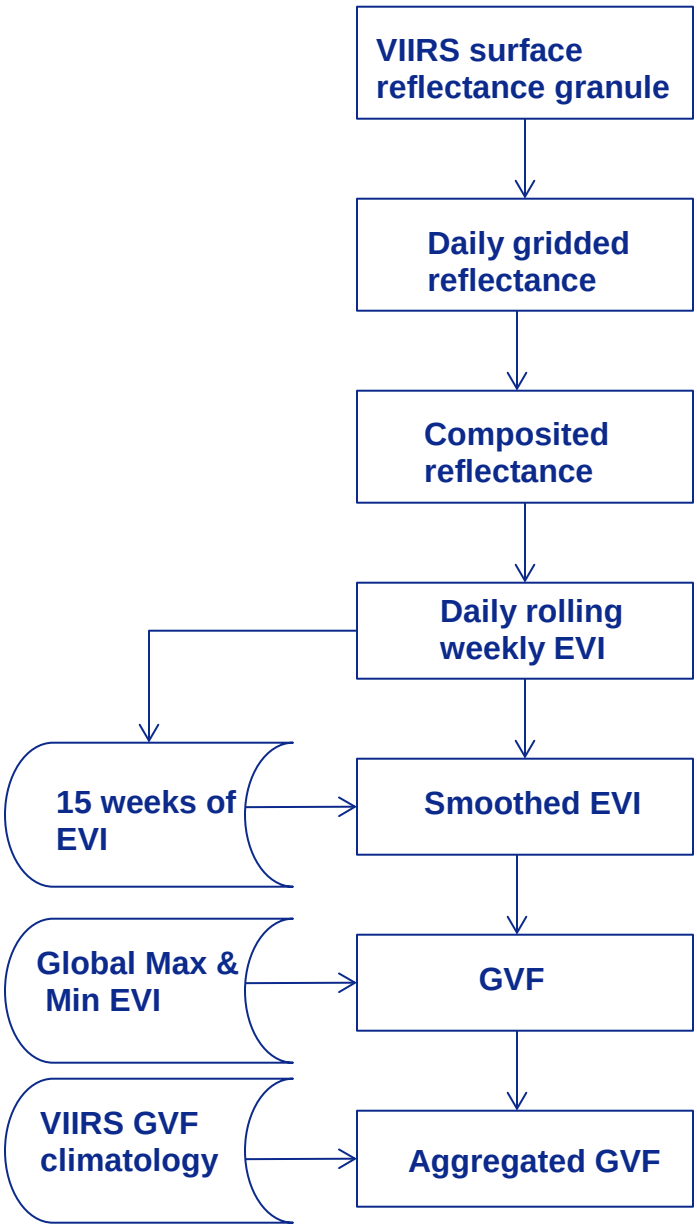

Figure 1. Flow chart of GVF system.

In Figure 1:

"VIIRS surface reflectance granule" is the surface reflectance in VIIRS bands I1, I2, and M3 for a VIIRS granule, obtained from the IVISR file.

"Daily gridded reflectance" is "VIIRS surface reflectance" projected to the native GVF grid during a calendar day.

"Composited reflectance" is the daily rolling weekly composite reflectance that is produced daily by Maximum Value Compositing of "daily gridded reflectance" in a 7-day period. This consists of the maximum view-angle adjusted SAVI value selected observation for each grid point (pixel)

"Daily rolling weekly EVI" is the EVI calculated from the daily rolling weekly composited reflectance in bands I1, I2, and M3.

"15 weeks of EVI" is the 15 non-overlapping daily rolling weekly EVI accumulated in the recent 15 weeks.

"Smoothed EVI" is the weekly EVI with high frequency noise removed by a 15-week digital filter.

"GVF" is the green vegetation fraction on the 0.003 degree grid, calculated from the smoothed EVI.

"Aggregated GVF" is the GVF aggregated to 0.009 degree and 0.036 degree grids

3.2 Algorithm Input

3.2.1 VIIRS surface reflectance data

The VIIRS surface reflectance Retained Intermediate Product *(*RIP) is a granule file (IVISR) that contains reflectance data in twelve VIIRS spectral bands listed in Table 1. The GVF algorithm uses the red (I1), NIR (I2) and blue (M3) reflectance data to calculate EVI and derive GVF from EVI. Could flag information is included in the IVISR files. Details of VIIRS surface reflectance RIP are available at http://npp.gsfc.nasa.gov/sciencedocuments/ATBD_122011/474-00034_VIIRS-SurfReflect-ATBD_Rev-_22Apr2011.pdf

3.2.2 VIIRS geolocation data

The VIIRS geolocation files (GITCO) include latitude and longitude and sun-view geometry information corresponding to the VIIRS Surface Reflectance RIP. The GVF algorithm uses the latitude and longitude information in gridding and the sun-view geometry information in compositing.

3.2.3 MODIS land mask

The Moderate Resolution Imaging Spectroradiometer (MODIS) 250-m land-water mask (MOD44W) was re-projected to the lat/lon projection and re-sampled to the GVF grid resolution (see section 3.3.1). The land-water mask is used as a static input of the GVF system to mask water pixels.

3.2.4 Global maximum and minimum EVI

The global minimum EVI (EVI_0) is the theoretical EVI value for bare soils where GVF=0 and the global maximum EVI (EVI_∞) is the theoretical EVI value for dense vegetation where GVF=1. Both are global constants, independent of vegetation and soil types. Based on the MODIS Aqua daily surface reflectance (MYD09GA) data in four months at different seasons (Feb, May in 2007 and Aug, Oct in 2006), the global values, EVI_0=0.0602 and EVI_∞=0.5707, were empirically estimated, taken as the 5^{th} and 95^{th} percentiles from the probability distribution function of the weekly EVI maps (Fig. 2). Cloud and snow/ice pixels are excluded in the calculation of the probability distribution function of EVI since there is no vegetation information in these pixels. The global values were updated based on SNPP VIIRS weekly EVI data between 8/1/2012 and 8/3/2013. The VIIRS EVI_∞ is 0.6766 and EVI_0 is 0.0900. These global maximum and minimum EVI values will be evaluated and updated after certain (3-5) years of operation of the GVF system.

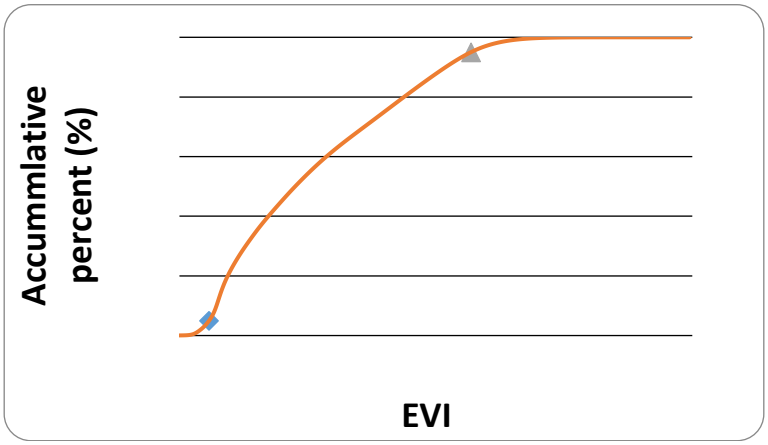

Figure 2. Global EVI accumulated probability distribution function of the weekly EVI maps in four months at different seasons.

3.2.5 GVF climatology

GVF climatology data are needed to fill gaps in high latitude areas in winter and potential gaps in other areas because of no input data. Global 0.036-degree and regional 0.009-degree monthly GVF climatology data are derived from daily rolling weekly EVI between 8/1/2012 and 8/31/2013, which is an intermediate variable of the GVF system (Fig. 1). Daily rolling weekly EVI data at 0.003-degree resolution are re-sampled to 0.036-degree and 0.009-degree resolutions. The maximum daily rolling weekly EVI value in each month is selected per pixel for the global and regional resolutions, respectively. It is monthly compositing of the EVI data. Monthly GVF is calculated from the monthly composite EVI data using Eq. (3.7).

There is no EVI data in high latitude areas in winter even after monthly compositing simply because of no sunlight. To retrieve green vegetation fraction over dark area, we combined the MODIS vegetation continuous field data (MOD44B) and the MODIS land cover data (MCD12Q1) to estimate the fraction of evergreen trees at high latitude area. Both MOD44B and MCD12Q1 are produced yearly, at nominally 250m and 500m resolutions respectively. The most recent vegetation continuous field product is for year 2010 and it only contains tree fractions at current stage. From the year 2010 land cover product (MCD12Q1), pixels with the evergreen needle-leaf, evergreen broad-leaf, and mixed forest land cover types are identified. MCD12Q1 data provide the land cover information, whereas the MOD44B data

provide the tree fraction information for each pixel. By combining these two products, tree fraction over the evergreen needle-leaf and evergreen broad-leaf pixels are assumed to be equal to GVF. For the case of mixed forest pixels, half of the tree fraction is assumed to be GVF. In theory, ever-green tree fraction is the GVF for cold regions where there is no other evergreen vegetation. A global MODIS evergreen tree fraction dataset is created using this method.

MODIS evergreen tree fraction data are re-sampled to the resolution of 0.036 and 0.009 degrees and used to fill the dark area at the high latitudes of the global and regional monthly GVF derived from the monthly EVI data. The global GVF climatology covers longitudes from -180° to 180° and latitudes from 90° to -90° and the regional GVF climatology covers longitudes from 130°E eastward to 30°E and latitudes from 90°N to 7.5°S. The global and regional monthly GVF climatology is used to fill any gaps over land pixels on daily rolling weekly GVF data.

The GVF climatology data will be evaluated and updated after certain (3-5) years of operation of the GVF system.

3.3 Theoretical Description of Retrieval GVF Method

Vegetation indices are spectral transformations of two or more bands designed to enhance the contribution of vegetation properties and allow reliable spatial and temporal inter-comparison of terrestrial photosynthetic activity and canopy structural variations (Huete et al., 2002). Many studies showed that NDVI is highly related to GVF (Jiang et al., 2006; Leprieur et al., 2000; Gutman and Ignatov, 1998; Carlson and Ripley, 1997; Baret et al., 1995; Wittich and Hansing, 1995). Some researchers found that there is a linear relationship between NDVI and GVF (Gutman and Ignatov, 1998; Wittich and Hansing, 1995; Kustas et al., 1993; Phulpin et al., 1990; Ormsby et al., 1987). But others found the NDVI-GVF relationship to be nonlinear since the sensitivity of NDVI decreases with the increase of vegetation density and becomes saturated easily (Jiang et al., 2006; Leprieur et al., 2000; Purevdorj et al., 1998; Carlson and Ripley, 1997; Baret et al., 1995; Dymond et al., 1992).

3.3.1 Gridding

The GVF system algorithm starts from VIIRS surface reflectance RIP granules and grid the data, using nearest-neighbor method, onto a global GVF 0.003° (333-m) grid. This grid is based on the Plate Carrée map projection and consists of 120,000×60,000 grid points (pixels)

in the global map, which spans from 90° (north edge) to -90° (south edge) in the latitudinal and from -180° (west) to 180° (east) in longitude directions.

3.3.2 Compositing

The GVF input includes the VIIRS surface reflectance RIP and geo-location data for each granule. Daily I1, I2, and M3 surface reflectance data in a seven-day period are composited at 1-day interval (daily rolling weekly). A daily rolling weekly compositing period can start at any day of a year and covers seven days. The next compositing period shifts one day after the last seven-day period. At the end of a year, a compositing period cover some days in the next year if there are not enough days left in the year. The end result of composting over a seven-day period is a single file containing, for each 0.003 degree grid point, red (I1), NIR (I2), and blue (M3) reflectance, sensor and solar zenith angles, relative azimuth angle in a NetCDF file.

The compositing procedure developed for the GVF system is different from the traditional maximum value compositing (MVC) procedure used in the GVPS system. It is well documented that MVC based on NDVI favors observations in the forward scatter direction, creating a bias and resulting in low red and NIR reflectances because of shadowing effect (Cabral et al., 2003; Carreiras et al., 2003; van Leeuwen et al., 1999; Stoms et al., 1997; Cihlar et al., 1994; Huete et al., 1992; Gutman, 1991). To reduce the bias, the soil-adjusted vegetation index (SAVI), with varying soil adjustment factor (L) values, is proposed and tested for MVC using the MYD09GA data (i.e. VIIRS surface reflectance proxy data) (Jiang et al., 2014). It was found that L had great impact on the selection of the composited data. With the increase of the L value from 0 to 0.5, the bias shifted from the forward scatter direction to the backscatter direction (Fig. 3). Mean EVI values composited based on SAVI are greater than those composited based on NDVI (L=0) (Fig. 4). The SAVI with L=0.05 was found to be the optimal vegetation index used in compositing to minimize the bias between the two directions (Fig. 3).

$$SAVI = (1+L)\frac{\rho_{NIR} - \rho_{red}}{\rho_{NIR} + \rho_{red} + L} \quad (3.1)$$

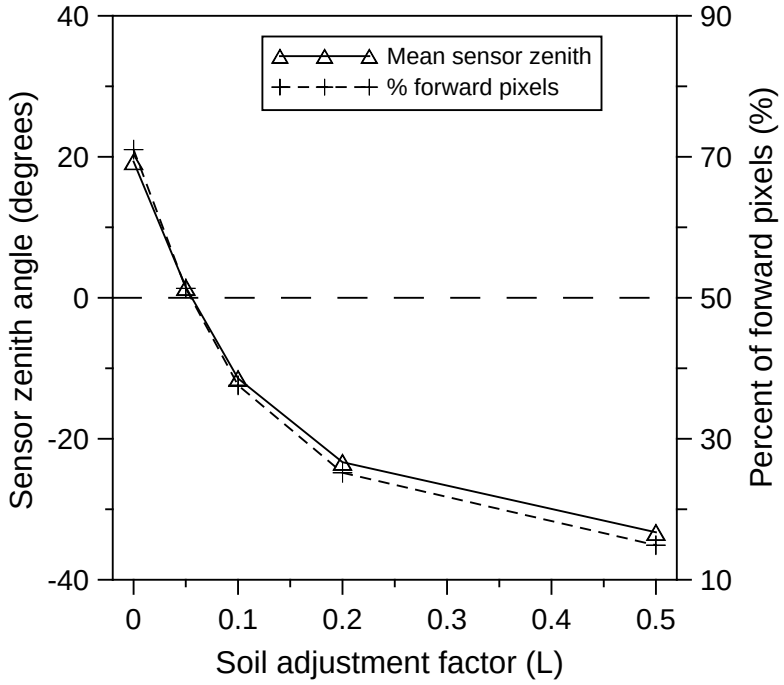

Figure 3. Yearly mean sensor zenith angles and yearly mean percentage of forward scatter direction pixels of the maximum SAVI composited images over the tile H10V05 in 2007 as functions of the soil adjustment factor (L) values.

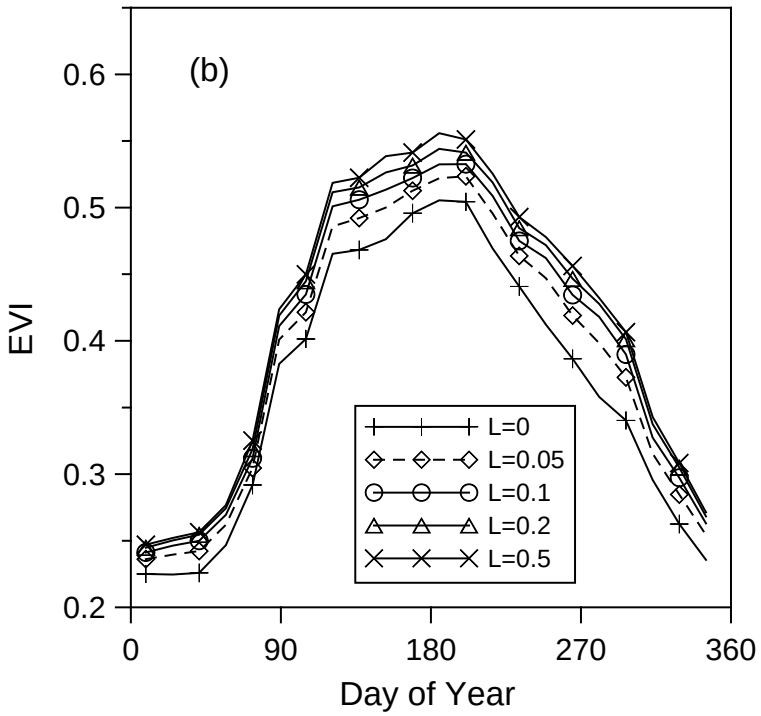

Figure 4. Mean EVI composited by the maximum SAVI method using the five soil adjustment factor (L) values over the tile H10V05 in 2007.

Although the bias in the view angle directions can be successfully minimized by the MVC based on SAVI (L=0.05), most of pixels composited by MVC are from high sensor zenith angles, regardless of whatever L values are used in compositing (Fig. 5). In some cases, the maximum NDVI is selected at the expense of optimal view geometry since sensor zenith angles selected by MVC are often further off-nadir than necessary to ensure cloud-free viewing (Stoms et al, 1997). This is an inherent limitation of MVC since more vegetation canopies and fewer gaps among canopies can be observed from high view zenith angles than from the nadir view.

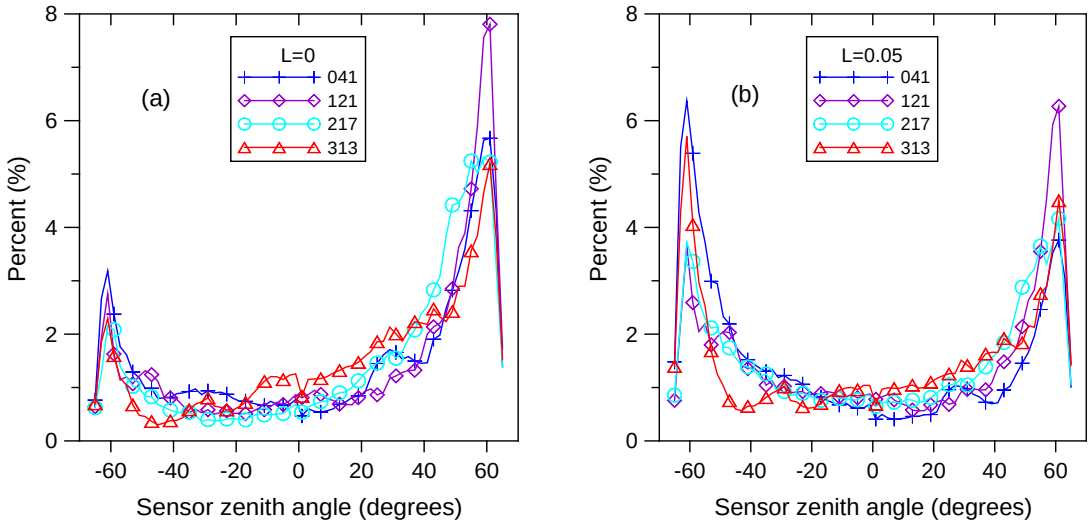

Figure 5. Histograms of the sensor zenith angles composited by the traditional MVC based on NDVI (L=0) (a) and by the MVC based on SAVI (L=0.05) in different seasons (compositing periods beginning at DOYs 041, 121, 217 and 313) in 2007 over the tile H10V05.

Thus, sensor zenith angles should be taken into account in compositing such that observations close to the nadir view are given a priority under clear sky conditions and observations at off-nadir view should be selected only if nadir view observations are cloudy. So, in compositing, SAVI should be adjusted according to the sensor zenith angle for each observation. The view-angle adjusted SAVI (VA-SAVI) is

$$\text{VA-SAVI} = \text{SAVI} - C \times SZ^2 \quad (3.2)$$

where SZ is the sensor zenith angle in degrees and C is a coefficient that accounts for the view angle variation of SAVI. The view angle variation of SAVI and other VIs is associated with the bidirectional reflectance distribution function (BRDF) of surface. The BRDF effects are prominent over heterogeneous surface with intermediate vegetation density and insignificant over homogeneous surface, such as bare soil or fully vegetated area. So C is a function of vegetation density, which can be estimated by the maximum SAVI ($SAVI_{max}$) in a compositing period for a pixel.

$$C = C_1 - C_2(SAVI_{max} - 0.5)^2 \quad (3.3)$$

Where C_1=0.00008 and C_2=0.0002. The C value is highest (0.00008) when $SAVI_{max}$=0.5 and becomes 0.3 when $SAVI_{max}$=1 or 0 (Fig. 6). It should be noted that the C values are very small because the unit of sensor zenith angles in Eq. 3.2 is the degree.

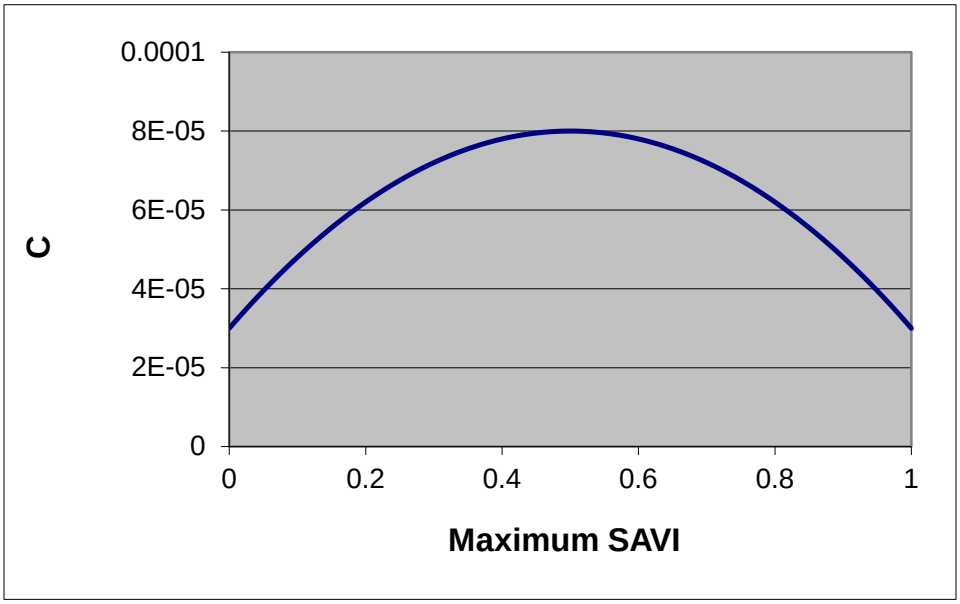

Figure 6. C is designed as a function of the maximum SAVI.

Instead of selecting the maximum NDVI, the GVF compositing algorithm selects the maximum view-angle adjusted SAVI (MVA-SAVI) in a compositing period for each pixel. Fig. 7 shows an example of the MVA-SAVI composing, compared with the traditional MVC. In the compositing period, only one day of observation is cloudy and the other six days are cloud-free. MVC selects the maximum NDVI observation at sensor zenith angle 52° in the forward scatter direction. Whereas the MVA-SAVI compositing method selects the observation closest to the nadir view since VA-SAVI values are reduced according to the sensor zenith angles. The higher sensor zenith angles, the smaller VA-SAVI values.

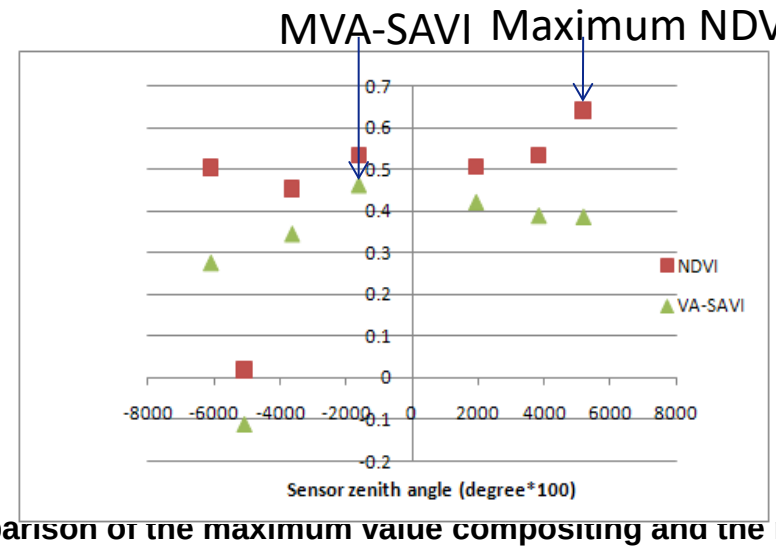

Figure 7. Comparison of the maximum value compositing and the maximum view angle adjusted SAVI compositing.

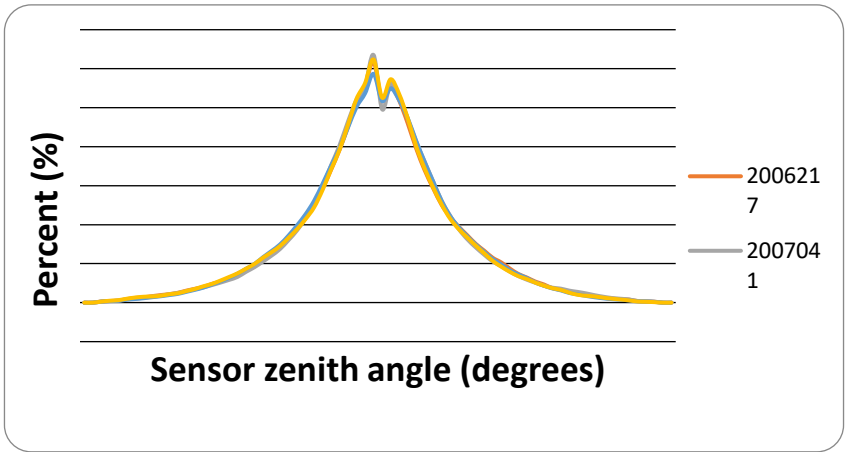

Figure 8. Histograms of sensor zenith angles composited by the MVA-SAVI method at different seasons.

The peaks of the histograms of sensor zenith angles composited by the MVA-SAVI method are close to the nadir at different seasons, indicating that observations close to the nadir view are likely selected than the off-nadir observations (Fig. 8).

3.3.3 EVI calculation

Gutman and Ignatov (1998) derived GVF from AVHRR NDVI based on a linear relationship between NDVI and GVF:

$$GVF = (NDVI - NDVI_0) / (NDVI_\infty - NDVI_0) \quad (3.4)$$

where $NDVI_0$ and $NDVI_\infty$ are the NDVI values for bare soil and dense green vegetation respectively. The current GVPS was developed in NOAA/STAR to generate real-time weekly 16-km global GVF from AVHRR GVI data based on the Gutman and Ignatov's method (Jiang et al., 2010). Details of GVPS are available at http://www.star.nesdis.noaa.gov/smcd/emb/vci/gvps/index.php

Since the current GVPS is based on the Top of Atmosphere (TOA) NDVI from AVHRR, there is a need to develop a new GVF product from NPP-VIIRS data in the SNPP era. With the availability of the blue bands, EVI data can be produced from the VIIRS sensor, in additional to the NDVI data. EVI was developed to optimize the vegetation signal with improved sensitivity in high biomass regions and improved vegetation monitoring through a de-coupling of the canopy background signal and a reduction in atmosphere influences. The equation takes the form,

$$EVI = G\frac{\rho_{NIR} - \rho_{red}}{\rho_{NIR} + C_1\rho_{red} - C_2\rho_{blue} + L} \quad (3.5)$$

where ρ_{NIR}, ρ_{red}, ρ_{blue} are the top of canopy (TOC) NIR, red and blue reflectances respectively, L is the canopy background adjustment that addresses nonlinear, differential NIR and red radiant transfer through a canopy, and C1, C2 are the coefficients of the aerosol resistance term, which uses the blue band to correct for aerosol influences in the red band. The coefficients adopted in the EVI algorithm are, L=1, C1=6, C2 = 7.5, and G (gain factor) = 2.5 (Huete, et al., 2002; Liu and Huete, 1995).

EVI not only gains its heritage from the soil-adjusted vegetation index (SAVI) (Huete, 1988) and the atmospherically resistant vegetation index (ARVI) (Kaufman and Tanré, 1994), but also improves the linearity with vegetation biophysical parameters, encompassing a broader range in leaf area index (LAI) retrievals (Houborg et al., 2007). It has been shown to be strongly linear related and highly synchronized with seasonal tower photosynthesis measurements in terms of phase and amplitude, with no apparent saturation observed over temperate evergreen needleleaf forests (Xiao et al., 2004), tropical broadleaf evergreen

rainforests (Huete et al., 2006), and particularly temperate broadleaf deciduous forests (Rahman et al., 2005; Sims et al., 2006).

EVI values are calculated from the weekly composited VIIRS red (I1), NIR (I2), and blue (M3) reflectance, using Eq. 3.5. Due to the use of blue band, the denominator of the EVI equation could be equal to, or very close to, 0 and EVI values are abnormal under certain circumstance. For example, when ρ_{red} =0.2380, ρ_{NIR}=0.2255 and ρ_{blue}=0.3538, the EVI value becomes infinite. A two-band EVI (EVI2) without a blue was developed by Jiang et al. (2008), which is robust under any circumstance and has the best similarity with the 3-band EVI.

$$EVI2 = 2.5\frac{\rho_{NIR} - \rho_{red}}{\rho_{NIR} + 2.4\rho_{red} + 1} \tag{3.6}$$

If the red/blue ratio is less than 1.25, or the blue reflectance is larger than 0.3, or EVI is larger than 0.7 or smaller than 0, then the EVI values are replaced by EVI2 values calculated using Eq. (3.6).

3.3.4 EVI time series smoothing

Cloud, ozone, dust, and other aerosols generally reduce the contrast of NIR and red reflectance over vegetated surface observed from space, which leads to undesirable variation in vegetation index products (Goward et al., 1991; Holben, 1986). Variation in viewing and sun geometry can lead to variation of EVI time series due to the BRDF effects of land surface. Sims et al. (2011) observed that EVI was highest for large view angles in the backscatter direction and lowest for larger view angles in the forward scatter direction and conclude that EVI was significantly affected by view angle variations.

To reduce the high frequency noise in the EVI time series caused by the cloud, aerosol and BRDF effects, the smoothing method used in the NOAA Vegetation Health Product (VHP) system is adapted (http://www.star.nesdis.noaa.gov/smcd/emb/vci/VH/index.php). The idea was to (a) single out the seasonal cycle; (b) suppress high frequency noise, and (c) enhance medium and low frequency variations related to large-scale and persistent weather fluctuations. This technique considers smoothing the weekly time series with a combination of a compound median filter and the least squares technique (Kogan et al., 2011; Sullivan, 1993; Kogan et al. 1990). The detail of the least squares technique for time series smoothing can be found in the technical report by Sullivan (1993).

However, we found the smoothing filter developed by Sullivan (1993) is not ideal for smoothing real time data because it can postpone the seasonality of the time series after

smoothing. Savitzky and Golay (1964) found that the least squares fitting calculations can be carried out by convolution of the data points with a filter and then provided a simplified method for calculating smoothing of time series data by a least square technique. However, the limitation of the technique is that it can only smoothing the middle point of data in a 2m+1 point filter and truncates the time series of data by m points at each end (Gorry, 1990), which means the technique cannot be used to smooth the latest (real time) data point in a time series. To overcome this problem, Gorry (1990) extended the convolution technique to cover all points in a time series based on the recursive properties of Gram polynomials. In the GVF system, the Gorry filter is used to replace the Sullivan filter (1993).

To smooth the current week of EVI, 14 weeks of previous weekly EVI time series are extracted for each pixel. Three steps are applied. (1) Gap filling. The missing EVI value in the 15 weeks of the EVI time series, mostly due to cloud contamination, are interpolated. (2) Median filtering. 5-point median filter is applied to the EVI time series. (3) Applying Gorry filter. To smooth the current week of EVI, 15 weeks of EVI values are convoluted with the Gorry filter.

3.3.5 GVF calculation

GVF values are calculated from smoothed weekly EVI. With the improved linearity and sensitivity in high biomass regions, EVI is suitable to derive GVF. The suitability of EVI for estimation of GVF based on the Gutman and Ignatov's method was tested and compared with the heritage TOA NDVI and TOC NDVI using the MYD09GA data (see section 3.5.1). It was found that GVF derived from EVI has a smaller error and bias than those derived from TOA NDVI and TOC NDVI. Therefore, the GVF algorithm uses the following equation to derive GVF from TOC EVI data:

$$GVF = (EVI - EVI_0) / (EVI_\infty - EVI_0) \quad (3.7)$$

where EVI_0 and EVI_∞ are the global minimum and maximum EVI as described in section 3.2.4. The equation is modified from the Gutman and Ignatov's method.

For pixels with EVI values greater than EVI_∞, the GVF values will be set as 1. Similarly, when $EVI<EVI_0$, then GVF=0.

3.3.6 GVF aggregation

The GVF previously calculated at the 0.003° grid is aggregated 3x3 to a 0.009° grid (~ 1 km) for output to regional 1km files. After aggregation, if there are missing GVF values over land pixels, particularly in high latitude area in winter, the regional monthly GVF climatology is used to fill the missing GVF values in the regional 1-km GVF files.

The GVF previously calculated at the 0.003° grid is aggregated 12x12 to a 0.036° grid (~ 4 km) for output to global 4km files. After aggregation, if there are missing GVF values over land pixels, then the global monthly GVF climatology is used to fill the missing GVF values in the global 4-km GVF files to ensure there is no gap in the output files.

3.4 Algorithm Output

The outputs of Green Vegetation Fraction Processing (GVF) system include:

(1) Daily rolling weekly 4-km GVF on a global geographic projection grid stored in a NetCDF file and a GRIB2 file, respectively.
(2) Daily rolling weekly 1-km GVF regional maps in geographic projection stored in a NetCDF file and a GRIB2 file.
(3) Color-coded browse images of the global and regional GVF maps, stored in Geo-TIFF files.
(4) Metadata: GVF statistical data (maximum, minimum, mean and standard deviation over selected areas), which are useful for OSPO to monitor the GVF product data quality and processing status, are saved in text files.

It should be noted that the GRIB2 files are converted from NetCDF files by a NetCDF4 to GRIB2 conversion tool (N4RT). GVF system does not produce GRIB2 files directly.

3.5 Performance Estimates

By using the weekly composited EVI data and comprehensive digital filters, the GVF system can produce Green Vegetation Fraction for the global area for each daily rolling week.

3.5.1 Test cases

To test the performance of the EVI-based GVF algorithm, NDVI is used to produce GVF and compared with EVI-derived GVF. Weekly GVF data were produced using the Gutman and Ignatov's method (Eq. 3.4) from TOA NDVI and TOC NDVI, respectively. Weekly TOA and TOC NDVI were composited using the traditional MVC method. Four months of weekly GVF data were produced based on the three different vegetation index datasets, i.e. TOA NDVI, TOC NDVI and EVI, respectively. Reference GVF data were derived from 129 Landsat/ETM+ images distributed globally over 30 EOS land validation core sites (Fig. 9) and in different seasons using a decision-tree classification method. The EOS Land Validation Core Sites are intended as a focus for land product validation over a range of biome types (http://landval.gsfc.nasa.gov/coresite_gen.html).

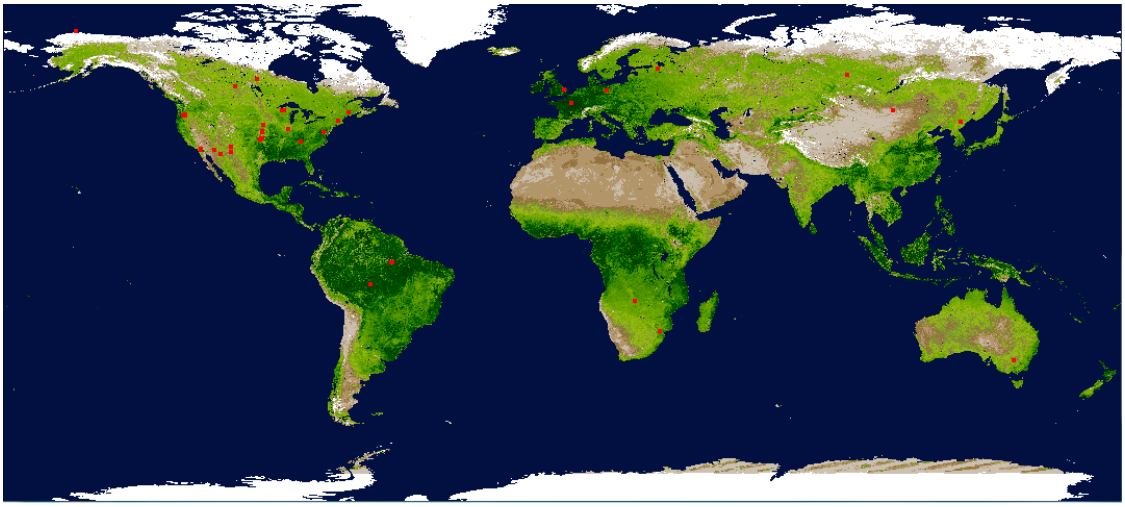

Figure 9. Location of EOS land validation core sites.

The classification tree is a robust classifier with good accuracy and has been used to generate the standard MODIS land cover classification MOD12 (Friedl et al. 2002) and MODIS vegetation continuous field MOD44 (Hansen et al. 2002). The routine *rpart* in the open-source statistical package ***R*** is used to generate the classification tree rules from the training data. The R rules are then implemented as a C function to classify the Landsat data for efficiency. Fig. 10 shows the classification map. Green agricultural lands and natural vegetation areas are classified as vegetation successfully by visual examination.

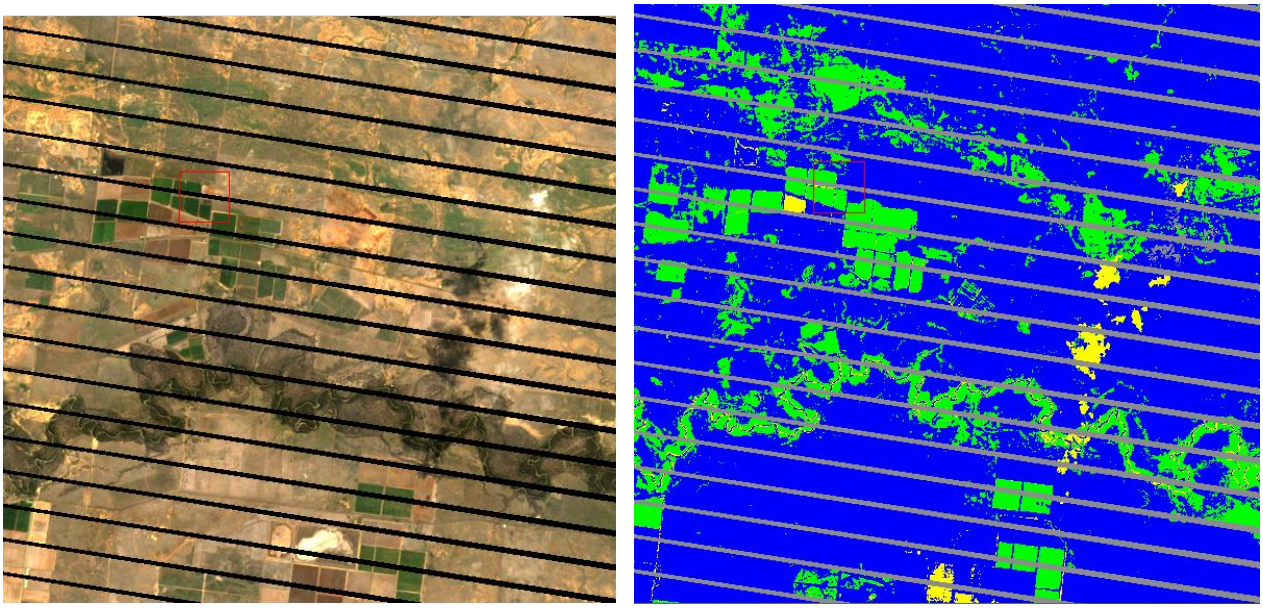

(a) (b)

Figure 10. Landsat true color image (a) and the classification map (b). Green: vegetation; Blue: bare soil; Yellow: cloud.

The Landsat classification maps were re-projected to the 4-km geographic projection grid. Percent of vegetation pixels in each 4-km grid were calculated and compared with the GVF data derived from TOC EVI, TOC NDVI and TOA NDVI. The comparison of the three GVF derived from the MODIS data and the Landsat classified GVF are shown in Fig. 11 and table 2. Accuracy and the mean absolute difference between the VI derived GVF and the Landsat derived GVF were calculated using Eq. 3.8 and Eq. 3.9, respectively. Accuracy is defined as the magnitude of the mean error. It is showed that GVF values derived from TOA NDVI and TOC NDVI are overestimated when GVF is less than 0.4, resulting in large accuracies (Table 2). The TOC EVI derived GVF has least error and accuracy than the other two GVF products, which suggests that the GVF algorithm perform better than the traditional GVF algorithm based on NDVI composited by MVC.

Note that the test case analyses retrieved GVF from unsmoothed vegetation indices, while the operational algorithm will retrieve GVF from smoothed EVI. We do not expect this difference to invalidate our conclusion that TOC EVI is the better index because we only use clear-sky observations in the comparison of MODIS GVF and Landsat GVF.

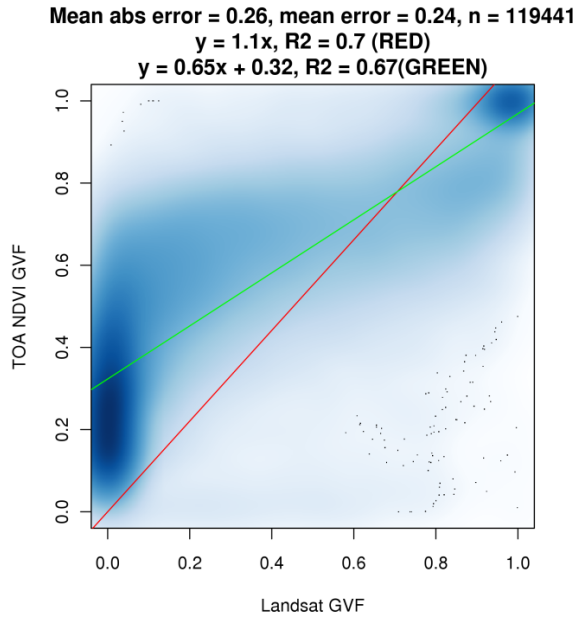

(a)

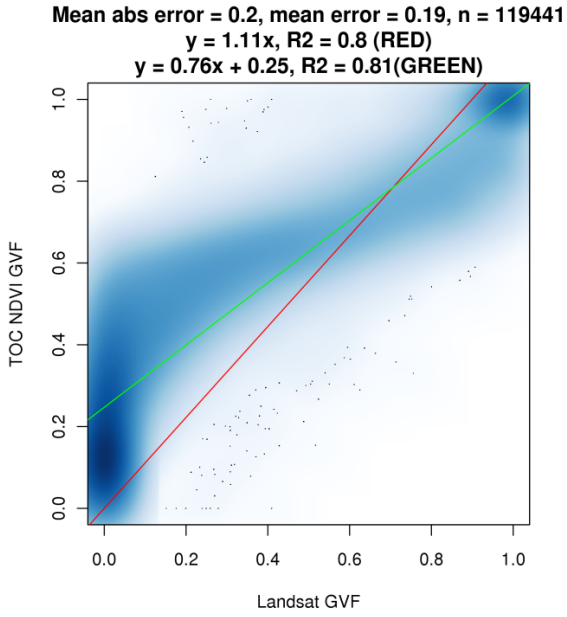

(b)

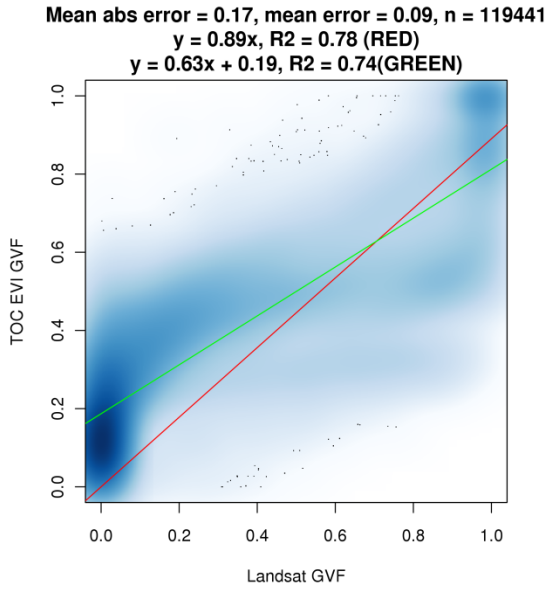

(c)

Figure 11. Scatter plots of the GVF derived from (a) TOA NDVI, (b) TOC NDVI and (c) TOC EVI versus Landsat classified GVF.

Table 2. Mean absolute error and Accuracy of the GVF derived from weekly VIs compared with the Landsat classified GVF.

	Mean absolute error	Accuracy
GVF from TOA NDVI	0.26	0.24
GVF from TOC NDVI	0.20	0.19
GVF from TOC EVI	0.17	0.09

n=119441. All 4-km pixels have less than 5% cloud coverage.

$$\text{Mean absolute error} = \frac{1}{n}\sum \left| GVF_{VI} - GVF_{Landsat} \right| \quad (3.8)$$

$$\text{Accuracy} = \frac{1}{n}\left| \sum \left(GVF_{VI} - GVF_{Landsat} \right) \right| \quad (3.9)$$

3.5.2 Sensor Radiometric Performance

The S-NPP was launched on October 28, 2011. Following a series of spacecraft and sensor activation and checkouts, the first VIIRS image was acquired on November 21, 2011, and all 22 VIIRS bands were producing early images by January 20, 2012. Since launch, the VIIRS SDR calibration/validation has been progressing well. A team of experts from NOAA, NASA, the Aerospace Corporation (Aerospace), University of Wisconsin, MIT/Lincoln Laboratory, and other industry partners have worked intensively and performed a thorough evaluation of the VIIRS on-orbit performance with 58 cal/val tasks. These tasks include 7 tasks for Functional Performance & Format evaluation (FPF), 7 tasks for Calibration System Evaluation (CSE), 4 tasks for Image Quality Evaluation (IQE), 25 tasks for radiometric evaluation (RAD), 9 tasks for Geometric Evaluation (GE), and 5 tasks for Performance and Telemetry Trending (PTT). Descriptions of these tasks can be found in the VIIRS SDR Operational Concept (OPSCON) document (DeLuccia and Cao, 2011). The VIIRS instrument post-launch calibration/validation process undergoes three phases: Early orbit checkout (EOC), Intensive Calibration/Validation (ICV), and Long-term Monitoring (LTM). Typically, EOC is the first 3-6 months after the instrument is turned on. ICV is the period from the end of EOC to plus approximately 2-6 months. LTM is the period from the end of ICV

until the end of the mission when the data is mature for operational use, although anomalies and upgrades are still expected (Cao et. al., 2013).

3.5.3 Sensor Radiometric Calibration

To meet the radiometric performance requirements through the entire mission, onboard calibration devices are essential for VIIRS. The calibration source for RSB (Reflective Solar Bands) is a full aperture SD (Solar Diffuser) that is illuminated once per orbit as the satellite passes from the dark side to the sunlit side of the earth in the high latitudes of the southern hemisphere. An attenuation screen covers the opening, but there is no door or other optical element between the SD and the sun. The Bidirectional Reflectance Distribution Function (BRDF) of the SD and the transmittance of the attenuation screen are measured pre-launch and verified on-orbit through observations made during spacecraft maneuvers. Given the angles of incidence, the reflected solar radiance can be computed and is used as a reference to produce calibrated reflectance and radiance. The space view (SV) provides the offset measurements needed for the calibration. Based on post-launch calibration/validation, the VIIRS SD is stable over most of the visible and near-infrared spectrum but shows a moderate degradation towards the blue spectral region. For example, an ~10% SD degradation has been observed for the first six months in the 0.412 m spectral region, primarily due to ultraviolet radiation on the SD, while little degradation is observed in the longer wavelength such as the 0.865um spectral region. This VIIRS SD degradation is more pronounced than that of Aqua MODIS which is ~2.6% per year at 0.412 μm mainly due to the more frequent SD exposure to the sun light since there is no SD door.

The SD degradation is monitored by the SD stability monitor (SDSM), which is a separate device with 8 detectors (from 0.412 μm to 0.926 μm). The faster degradation in the longer wavelength is likely due to preferential bombardment by high energy particles which affects more in the longer wavelength than in the shorter wavelength because these particles can penetrate deeper in the detector layers of the focal plane array. For the RSB, the calibration uncertainty in spectral reflectance for a scene at typical radiance is expected to be less than 2%. This performance has been demonstrated in pre-launch testing in the laboratory, but on orbit performance requires additional effort by using the onboard SD and vicarious calibration at desert and ocean sites, as well as inter-comparisons with other satellite instruments. Additionally, the monthly lunar calibration through a spacecraft roll maneuver is part of the post-launch calibration strategy to ensure that the sensor degradation is independently verified (Cao et. al., 2013).

3.5.4 Sensor noise Characterization

The pre-launch and on-orbit performance of the VIIRS visible and near-infrared bands are summarized in Table 3, which shows that the Signal-to-noise-ratio (SNR) or the noise-equivalent change in temperature (NEdT) for all VIIRS bands far exceeded the requirements and specifications. The Typical Radiance (Ltyp) values for each band are also presented in Table 3.

Post-launch results from on-orbit calibration data show that VIIRS noise performance is excellent, exceeding specifications for all bands. SNRs at typical scene radiance for the reflected solar bands (or RSB M1-M11, I1-I3, and DNB) are all more than 30% better than the specification, and several times better than specification for selected bands. For the RSB on-orbit performance, the SNR was derived from SD view and Space View (SV) observations. The Noise Equivalent Delta Radiance (NEdL) are computed using the SD and SV data as the standard deviation of the signal measured in digital number (DN) for the constant radiance scenes of either the SD or SV views. The NEdL and thus the SNR at Ltyp was then interpolated (extrapolated) from the NEdL at these known levels.

Table 3. Signal-to-noise-ratios of the VIIRS visible and near-infrared bands

Band No.	Driving EDR(s)	Spectral Range (um)	Horiz. Sample Interval (km) (track x Scan)		Band Gain	Ltyp or Ttyp (Spec)	Lmax or Tmax	Spec SNR or NEdT (K)	Prelunch SNR or NEdT (K)	On Orbit SNR or NEdT (K)
			Nadir	End of Scan						
M1	Ocean Color Aerosol	0.400 - 0.421	0.75 x 0.75	1.60 x 1.58	H	44.9	135	352	616	588
					L	155	615	316	1092	1045
M2	Ocean Color Aerosol	0.436 - 0.451	0.75 x 0.75	1.60 x 1.58	H	40	127	380	622	572
					L	146	687	409	1118	1010
M3	Ocean Color Aerosol	0.477 - 0.496	0.75 x 0.75	1.60 x 1.58	H	32	107	416	690	628
					L	123	702	414	1111	988
M4	Ocean Color Aerosol	0.541 -0.561	0.75 x 0.75	1.60 x 1.58	H	21	78	362	581	534
					L	90	667	315	963	856
I1	Imagery EDR	0.597 - 0.679	0.375 x 0.375	0.80 x 0.789	S	22	718	119	240	214
M5	Ocean Color Aerosol	0.662 - 0.680	0.75 x 0.75	1.60 x 1.58	H	10	59	242	366	336
					L	68	651	360	827	631
M6	Atmosph. Correct.	0.738 - 0.752	0.75 x 0.75	1.60 x 1.58	S	9.6	41	199	415	368
I2	NDVI	0.842 - 0.881	0.375 x 0.375	0.80 x 0.789	S	25	349	150	304	264
M7	Ocean Color Aerosol	0.843 - 0.881	0.75 x 0.75	1.60 x 1.58	H	6.4	29	215	519	457
					L	33.4	349	340	845	631

For the on-orbit performance, TEB NEdT is determined from the VIIRS instrument response to the OBC (On Board Calibrator) BB (Black Body) which operates at a nominal temperature of ~292K. The NEdL is computed at the blackbody temperature, interpolated to the specified Ltyp level, and then the NEdL is converted to its corresponding NEdT at Ttyp. It should be

noted that the NEdL values at blackbody and space views are comparable for the TEB. In other words, the noise is not a significant function of the amount of incoming radiation. Therefore, the NEdT at different scene brightness temperatures can be calculated using the Planck function (Cao et. al., 2013).

3.6 Practical Considerations

3.6.1 Numerical Computation Considerations

The whole algorithm is composed of many straight forward calculations, thus, it is light computationally.

3.6.2 Programming and Procedural Considerations

GVF code runs every day with all the available SNPP input data for making the daily composites and daily rolling weekly composites and produces the global and regional GVF products.

3.6.3 Quality Assessment and Diagnostics

Unit testing and system testing include quality assessment of the GVF products. Section 3.8 describes the validation of the VIIRS GVF product with the 30-m resolution Landsat GVF observations.

3.6.4 Exception Handling

The expected exceptions, and a description of how they are identified, trapped, and handled, are provided in the system maintenance manual.

3.7 Sample Results

Fig. 12 shows examples of the weekly VIIRS GVF maps in summer and winter. The GVF maps generally exhibit a good dynamic range from 0-1, indicating that this algorithm is capable of retrieving the required range of GVF values from the satellite sensor. The spatial patterns shown in the maps are also consistent with global dry/wet patterns of climate regimes and seasonal variations.

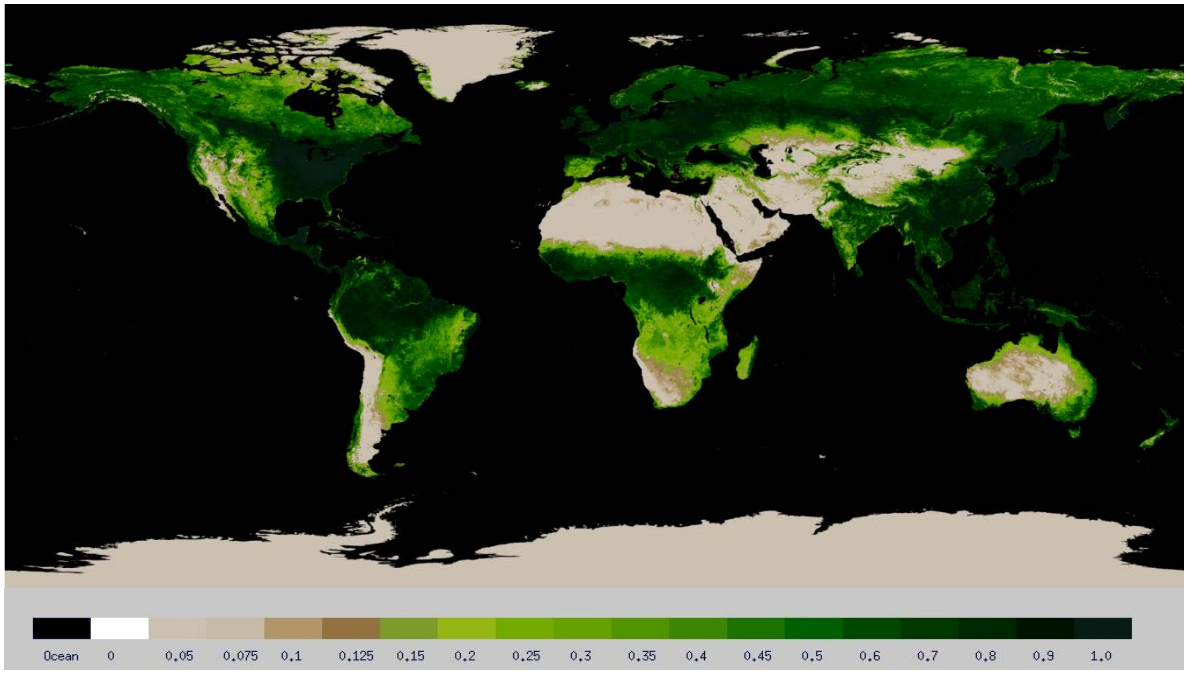
Ocean
0
0.05
0.075
0.1
0.125
0.15
0.2
0.25
0.3
0.35
0.4
0.45
0.5
0.6
0.7
0.8
0.9
1.0

(a)

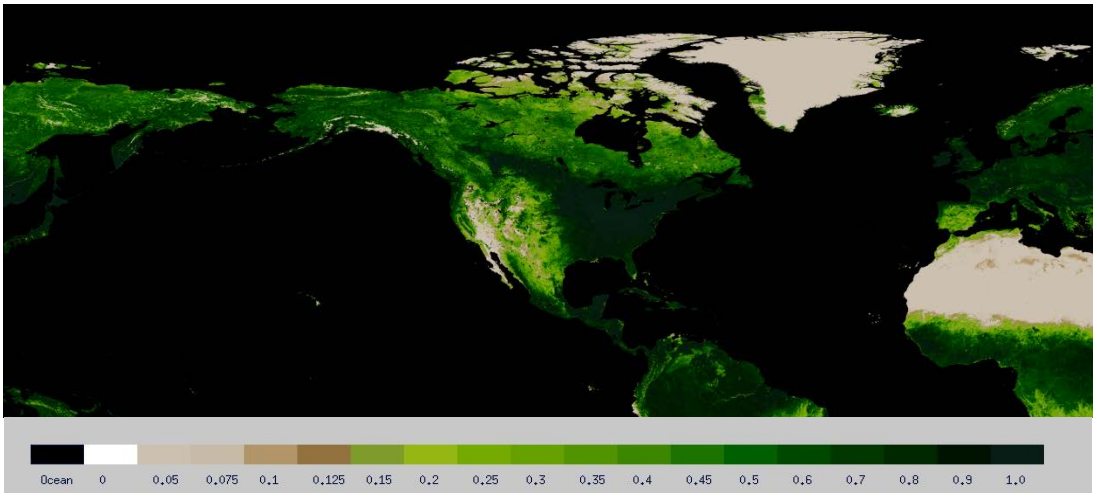
Ocean
0
0.05
0.075
0.1
0.125
0.15
0.2
0.25
0.3
0.35
0.4
0.45
0.5
0.6
0.7
0.8
0.9
1.0

(b)

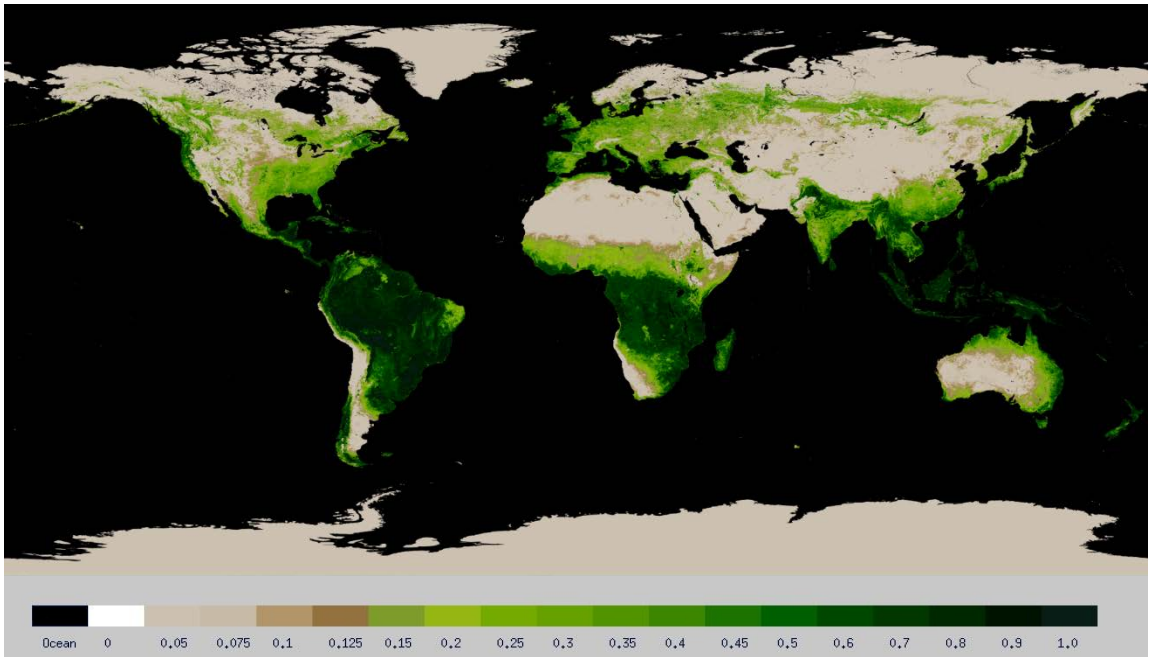

(c)

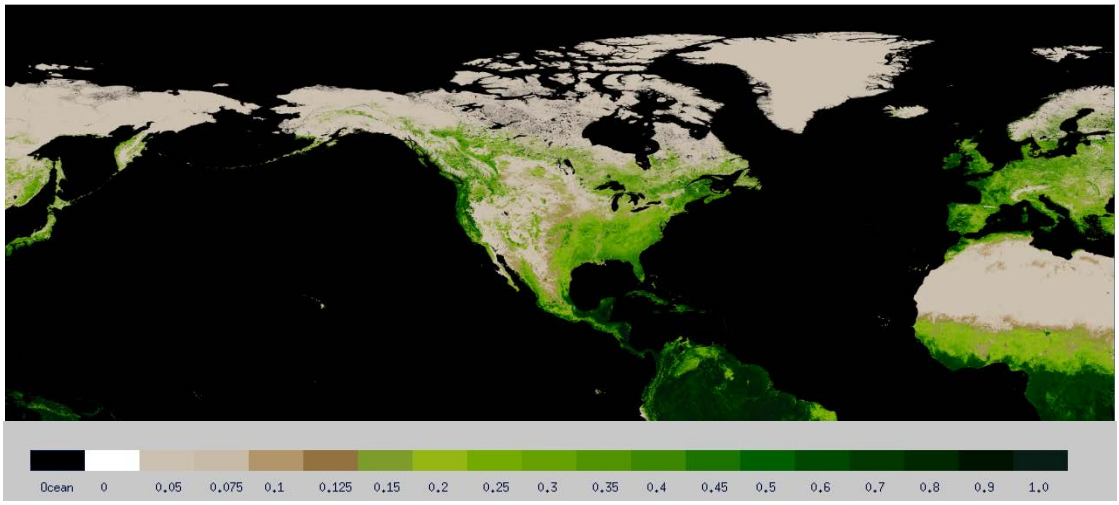

(d)

Figure 12. Daily rolling weekly Green Vegetation Fraction maps produced by the GVF system: (a) Global 4-km GVF for the week of 8/4/2013-8/10/2013 (b) Regional 1-km GVF for the week of 8/4/2013-8/10/2013, (c) Global 4-km GVF for the week of 2/14/2013-2/20/2013, and (d) Regional 1-km GVF for the week of 2/14/2013-2/20/2013.

Fig. 13 shows time series of daily rolling weekly GVF of the 4-km and 1-km pixels over three land cover types between 8/1/2012 and 9/18/2013. Great GVF variation was observed over Bondville and Konza Prairie (Fig. 13a & b), whereas low GVF values and small variation were observed over the desert area (Walnut Gulch) (Fig. 13c).

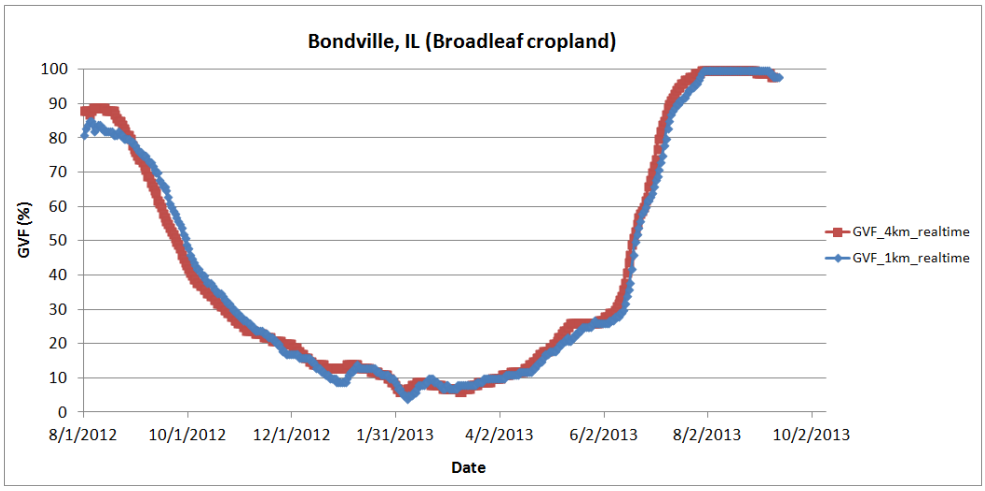

(a)

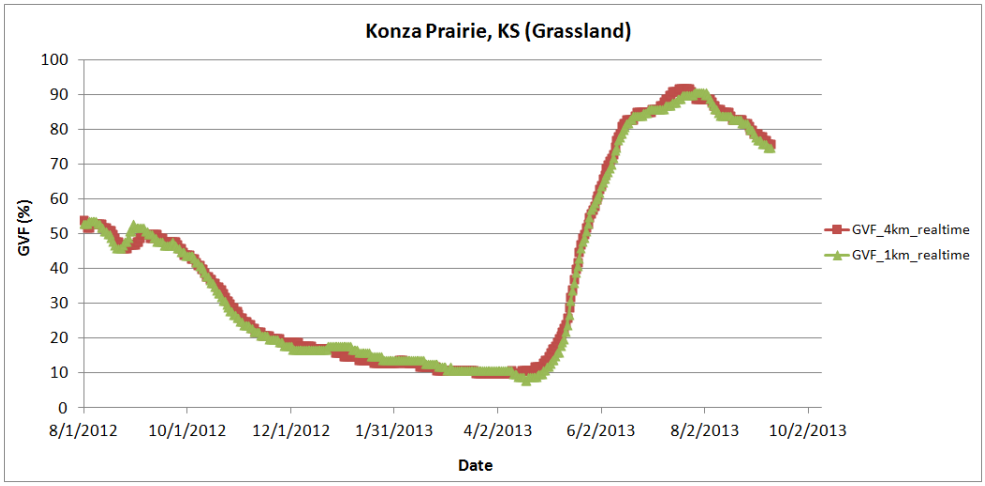

(b)

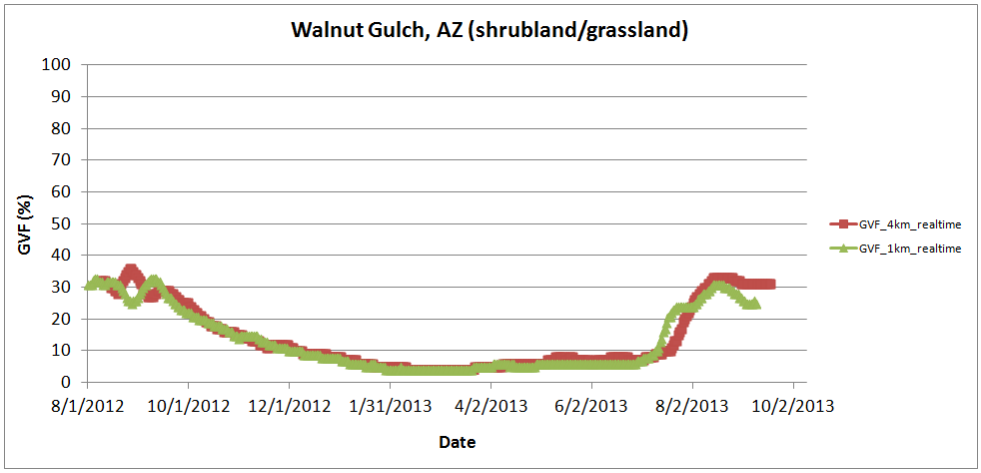

(c)

Figure 13. Time series of 4-km and 1-km daily rolling weekly GVF at (a) Bondville (lat 40.00°, lon -88.29°), (b) Konza Prairie (lat 39.08°, lon -96.56°) and (c) Walnut Gulch (lat 31.737°, lon -109.942°).

3.8 Validation Efforts

3.8.1 Validation using Landsat data derived GVF

For validation of the GVF algorithm, VIIRS GVF data between 9/1/2012 and 9/1/2016 were produced and validated with GVF "truth" data derived from Landsat data. With the spatial resolution of 30 meters in visible bands, the Landsat data can provide higher resolution vegetation information compared to the 4-km and 1-km GVF products. Therefore, the GVF derived from Landsat data is treated as "truth". 30 EOS Land validation core sites are selected globally (Fig. 9) and Lansat images covering these sites between 9/1/2012 and 9/1/2016 were downloaded from USGS (http://earthexplorer.usgs.gov/). Totally 126 high quality Landsat images were downloaded.

Landsat images were classified using the same classification tree method described in section 3.5.1. Four classes of training datasets were selected manually, representing vegetation, half-vegetation, bare surface and other non-vegetation (water, cloud, cloud shadow), respectively. All Landsat pixels were classified into the four classes. GVF values of vegetation, half-vegetation, bare soil pixels are counted as 100%, 50% and 0, respectively,

and the classification maps were converted to GVF maps. Other non-vegetation pixels were excluded in calculation of GVF and not used for validation. But the amount of non-vegetation pixels is used to indicate the quality of validation data since non-vegetation pixels do not provide any vegetation information.

Landsat GVF maps were re-projected to the 4-km and 1-km geographic projection grid. Land GVF in each 4-km and 1-km grid were calculated and compared with the VIIRS GVF. When there are more than 25% non-vegetation pixels within a VIIRS GVF pixel, the Landsat GVF of the 4-km or 1-km pixel was not considered in validation. A sample of an original Landsat image is shown in Fig. 14(a), where a gradient of vegetation density is shown from the suburban area to the center of the city. The classification image depicted the gradient of vegetation density from full vegetation in the suburban area to half-vegetation in urban area and to bare surface in the center of the city (Fig. 14b).

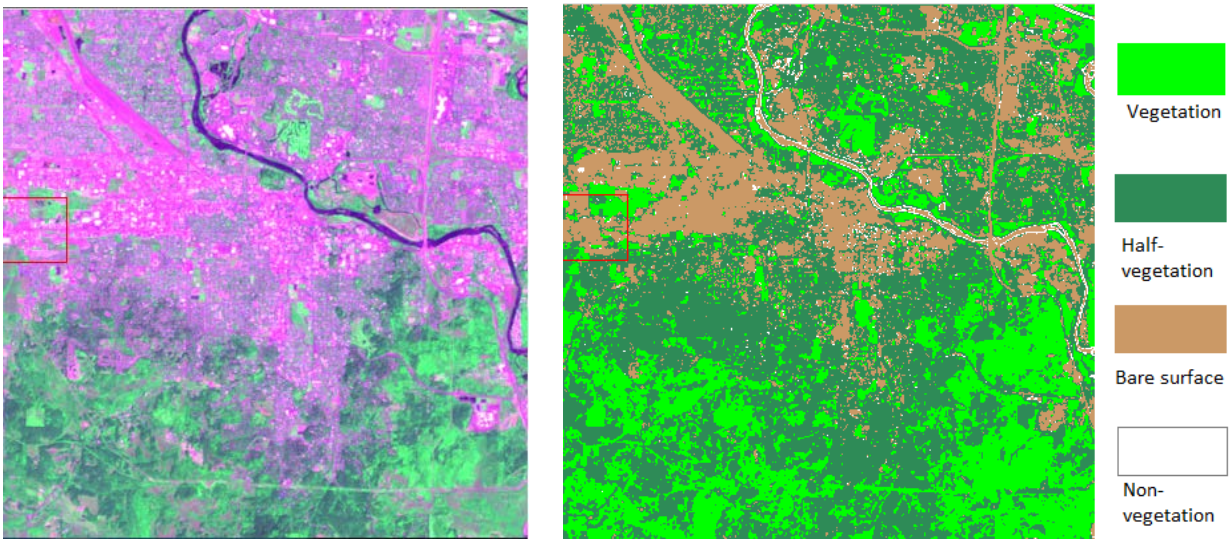

(a) (b)

Figure 14. (a) Landsat color image (red: band 3; green: band 4; blue: band 1) and (b) Lansat classification image with four classes, vegetation, half-vegetation, bare surface and non-vegetation.

Fig. 15 shows the scatter plots between Landsat derived GVF and VIIRS GVF at the 4-km and 1-km resolutions. There are totally 275,987 4-km VIIRS GVF pixels and 3,443,525 1-km VIIRS GVF pixels compared with Landsat derived GVF. The VIIRS GVF is correlated to

Landsat derived GVF very well and close to the 1:1 line, particularly for the VIIRS global 4-km GVF.

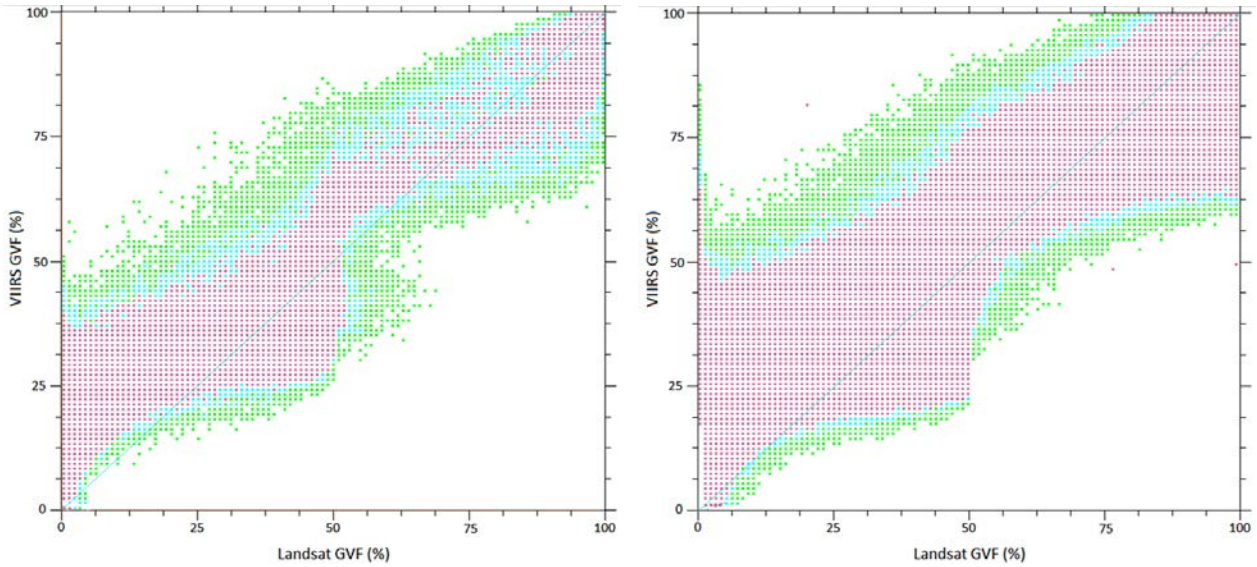

Figure 15. Scatter plots of (a) Landsat derived 4-km GVF against the 4-km VIIRS GVF and (b) Landsat derived 1-km GVF against the 1-km VIIRS GVF.

GVF measurement accuracy, precision and uncertainty are calculated according to Eqs 3.10-3.13. Accuracy is defined as the magnitude of the mean measurement error,

$$accuracy = |\mu| \tag{3.10}$$

where μ is the mean measurement error.

$$\mu = \sum_{i=1}^{n} \left(VIIR\_GVF_i - Landsat\_GVF_i \right) \tag{3.11}$$

Precision is defined as the standard deviation of the measurement errors.

$$precision = \left[\frac{1}{n-1} \sum_{i=1}^{n} \left(VIIR\_GVF_i - Landsat\_GVF_i - \mu \right)^2 \right]^{1/2} \tag{3.12}$$

Uncertainty is defined as the root mean square error (RMSE).

$$uncertainty = \left[\frac{1}{n} \sum_{i=1}^{n} \left(VIIRS\_GVF_i - Landsat\_GVF_i \right)^2 \right]^{1/2} \tag{3.13}$$

VIIRS GVF accuracy, precision and uncertainty are shown in Table 4. All the numbers are lower than the specifications, indicating that the global and regional VIIRS GVF products meet the design requirements.

Table 4. VIIRS GVF validation statistics

	Specifications (%)	VIIRS GVF (%)
Measurement accuracy		
Global	12	8.0
Regional	12	7.1
Measurement precision		
Global	15	8.4
Regional	15	7.0
Measurement uncertainty		
Global	17	11.6
Regional	17	10.0

3.8.2 Validation using GVF derived from Google Earth images

High resolution RGB color images with imagery dates are available on Google Earth. 30 sites including 15 Earth Observation Satellites land validation core sites (https://landval.gsfc.nasa.gov/) and 15 PhenoCam sites (https://phenocam.sr.unh.edu/) are selected. Most of the sites are located in U.S. The VIIRS GVF 0.036° grids that cover the 30 sites are identified and the latitude and longitude of the boundaries of grids are calculated. Google Earth images over the VIIRS GVF grids were downloaded from Google Earth image. The dates of the Google Earth images are observed from the bottom left side of Google Earth. The imagery date is recorded for each site. The corresponding VIIRS GVF pixel value is extracted on each site on the imagery date for comparison with GVF derived from Google Earth images.

The green pixels in the high resolution Google Earth RGB color images have higher digital numbers in the green channel than those in the red and blue channels. To identify the green pixels from non-green pixels in the high resolution Google Earth RGB color images, a green color index (GCI) is proposed by utilizing the difference between the digital number of the green channel and those of the red and blue channels.

$$GCI=3G-2R-B-20 \quad (3.14)$$

Where R, G, and B are the digital numbers of the red, green and blue channels of the image, respectively. The Google Earth pixels with positive GCI values are classified as green pixels and those with negative or zero GCI values are classified as non-green pixels. The GVF of the Google Earth image is calculated as the percentage of green pixels in the image. GVF derived from the Google Earth images are used as reference to compare with the VIIRS GVF.

Fig. 16a shows a high resolution Google Earth image acquired on Apr 27, 2017 over the Harvard forest site (lat 42.5393°, lon -72.1779°), which consists of 6912×9216 pixels, covering a VIIRS GVF pixel with an area of 0.036° by 0.036°. The pixels with positive GCI values are showed in bright green in Fig. 16b, which correspond to the green forest patches in the Google Earth image (Fig. 16a) every well. To take a close look at the Google Earth image, a small test area was chosen in the red rectangle in Fig. 16a and the full resolution image of the test area is shown in Fig. 16c. The individual tree canopies can be clearly seen in the high resolution Google Earth image (Fig. 16c). The classified image of the test area is shown in Fig. 16d. The green tree canopies and the green grassland were classified as green area successfully by utilizing the GCI method. The overall GVF of the Google Earth image at this site is 0.26. The corresponding VIIRS GVF on Apr 27, 2017 at this site is 0.34.

The GVF values derived from the high resolution Google Earth images over the 30 sites were plotted against the corresponding VIIRS GVF values in Fig. 17. The VIIRS GVF is closely related to the GVF derived from Google Earth images, with R^2=0.867. The VIIRS GVF is overestimated when GVF is less than 0.5 and underestimated when GVF is greater than 0.5 (Fig. 17). Further study is needed to investigate the optimal global maximum and minimum EVI values in Eq. 3.7. The accuracy, precision and uncertainty of the VIIRS GVF were 0.02, 0.1 and 0.1, respectively (Table 5).

(a)

(b)

(c)

(d)

Figure 16. Google Earth image covering a VIIRS GVF 0.036° grid at the Harvard forest site acquired on 4/27/2017 (a); classified image of the Google Earth image (b);

Google Earth image of the small area marked in the red rectangle in (a) (c); Classified image of the small area (d).

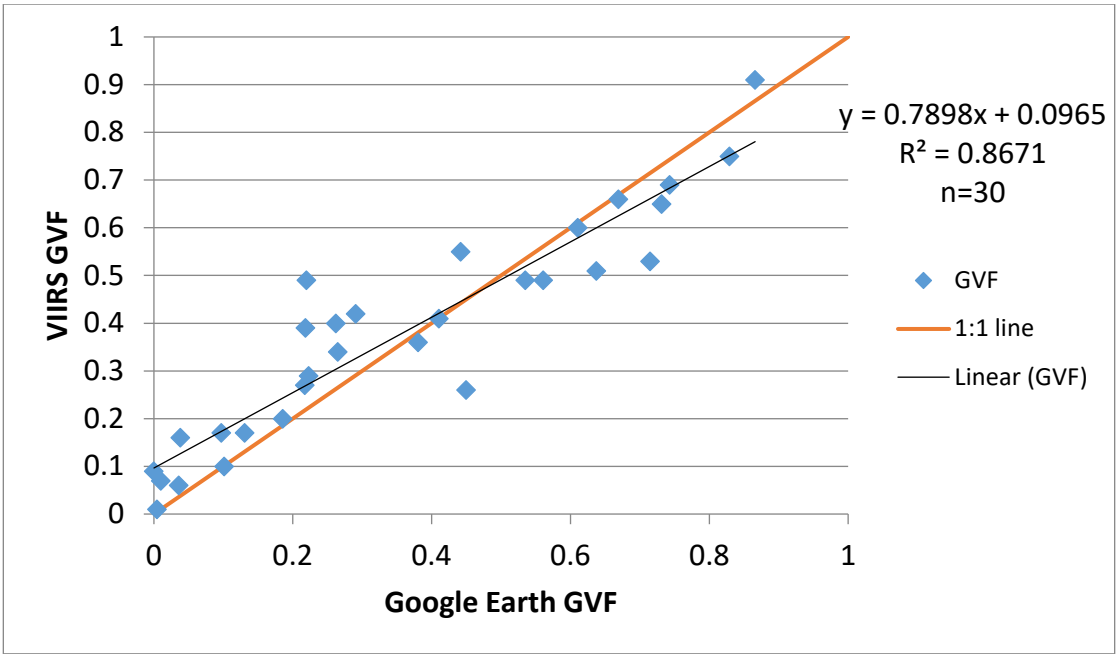

Figure 17. Scatter plots of Google Earth derived 4-km GVF against the VIIRS 4-km GVF.

Table 5. VIIRS 4-km GVF validation statistics using Google Earth images

	Specifications (%)	VIIRS GVF (%)
Measurement accuracy	12	2.0
Measurement precision	15	10.0
Measurement uncertainty	17	10.0

3.8.3 Validation of GVF seasonal variation using PhenoCam data

In order to validate the timing of the seasonal cycles of the VIIRS GVF data, we used the digital photos captured by high-resolution cameras (Webcams) from the PhenoCam network to derive ground phenology. The PhenoCam Network provides automated, near-surface RGB images of canopy phenology across the North America. Images are uploaded to the PhenoCam server every half hour. Ten PhenoCam sites in USA were selected in this study (Fig. 18). Daily PhenoCam images acquired at noon 12:00 were downloaded from PhenoCam website at https://phenocam.sr.unh.edu/webcam/network/download/.

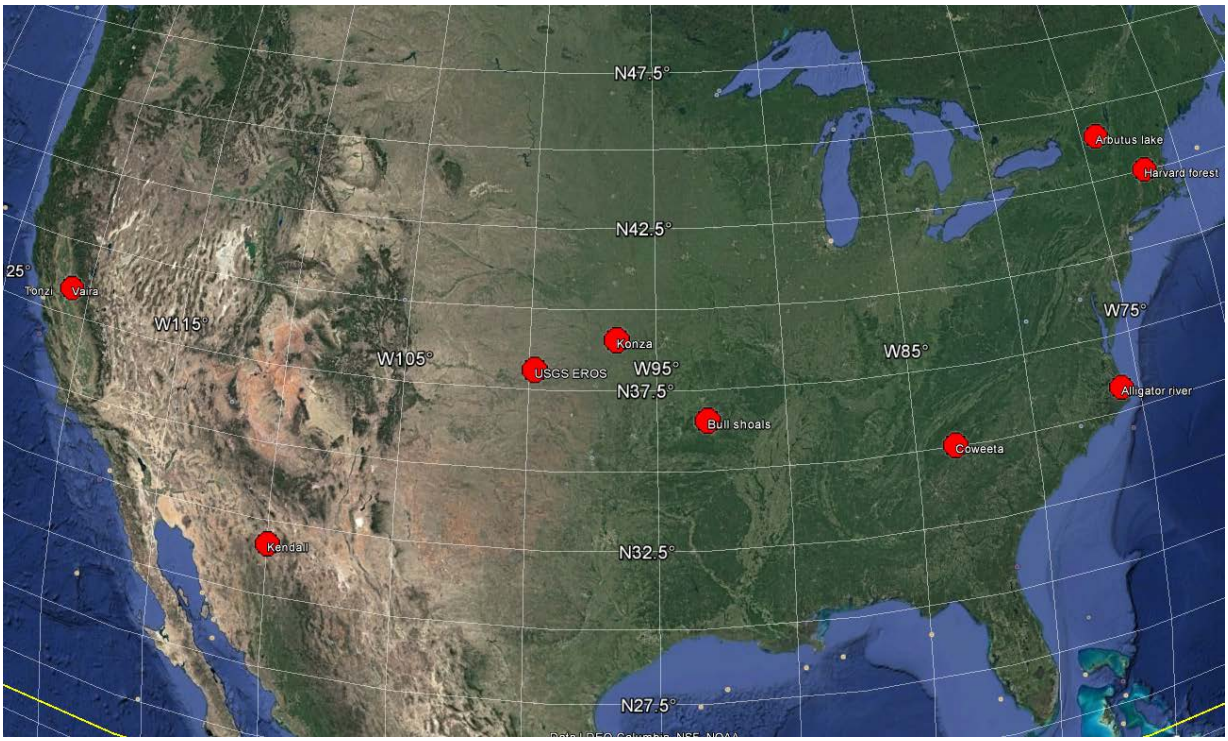

Figure 18. Location of the 10 PhenoCam sites selected for validation.

A region of interest (ROI), which includes vegetated surface close to the camera, was identified for each site. The digital numbers of the red (R), green (G) and blue (B) of the pixels within ROI were averaged. Green Chromatic Coordinate (GCC) was calculated based on the daily mean R, G, B values for each site (Klosterman et al 2014; Richardson et al 2009).

$$GCC=G/(R+G+B) \quad (3.15)$$

where R, G, B are the digital numbers of the red, green and blue channels, respectively. GCC measures the relative brightness of the green channel.

SNPP VIIRS 4-km Daily rolling weekly GVF data were extracted over 10 sites between September 2012 and December 2015. To compare with two previous NOAA GVF products, the operational NOAA-19 AVHRR 16-km weekly GVF data (Jiang et al 2010) were extracted over 10 sites between September 2012 and December 2015 and the 16-km monthly AVHRR GVF climatology data were also extracted over 10 sites.

The double logistic functions (Jeremy et al., 2006) was used to fit the time series of PhenoCam GCC, VIIRS GVF, AVHRR GVF and AVHRR GVF climatology

$$y(t) = \frac{c}{1+e^{a_1+b_1 t}} - \frac{c}{1+e^{a_2+b_2 t}} + d \qquad 3.16$$

where t is the time in days, y(t) is the GVF or GCC value at time t, a_1,a_2, b_1 and b_2 are fitting parameters, c+d is the maximum value, and d is the initial background value. The rate of change in the curvature of the fitted double logistic functions is used to identify phenological dates, including the dates of onset of leaf growth, maximum leaf area, senescence, dormancy and length of growing season according to the method of Zhang et al. (2003). The phonological dates correspond to the times at which the rate of change in curvature in the GCC or GVF time series reach local minima or maximums.

Daily GCC time series at Bull shoals in 2015 is shown in Fig. 19a. A double logistic curve is fitted to the GCC time series. The dates of onset of leaf growth, maximum leaf area, senescence, and dormancy are days of year (DOYs) 96, 121, 202 and 306, respectively. Time series of the VIIRS GVF, AVHRR GVF and the monthly AVHRR GVF climatology are shown in Figs. 19b-d. The phonological dates of the VIIRS GVF are closer to those of the ground measured GCC than the weekly AVHRR GVF and the monthly AVHRR GVF climatology (Fig. 19). The length of growing season of the VIIRS GVF time series is very close to that of GCC (Fig. 20). Whereas, the AVHRR GVF and the AVHRR GVF climatology have longer growing season than GCC.

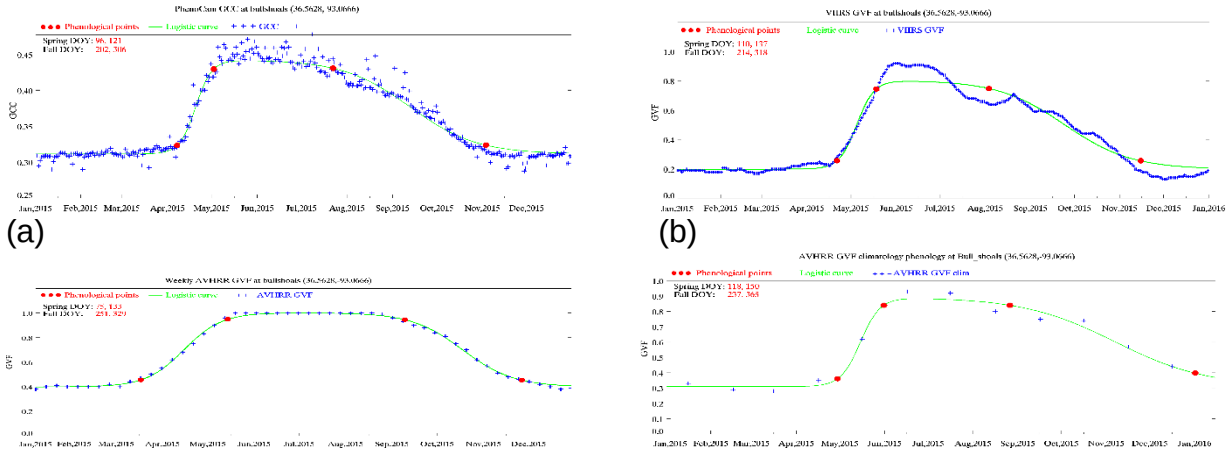

Figure 19. Time series of PhenoCam GCC (a), VIIRS GVF (b), weekly AVHRR GVF (c) and monthly AVHRR GVF climatology (d) at Bull shoals.

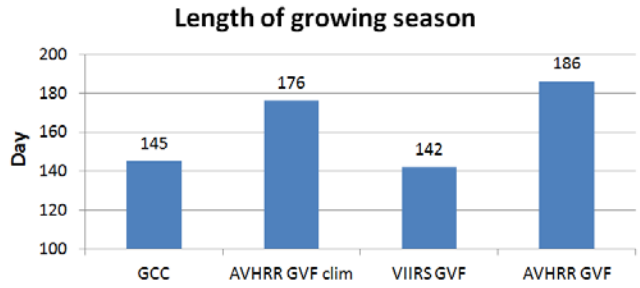

Figure 20. Comparison of the lengths of growing seasons.

The phenological dates of the VIIRS and AVHRR GVF products are compared with those of GCC over the 10 PhenoCam sites (Fig. 21). Overall, the phonological dates of the VIIRS GVF are closer to those of GCC in comparison with the AVHRR GVF and AVHRR GVF climatology.

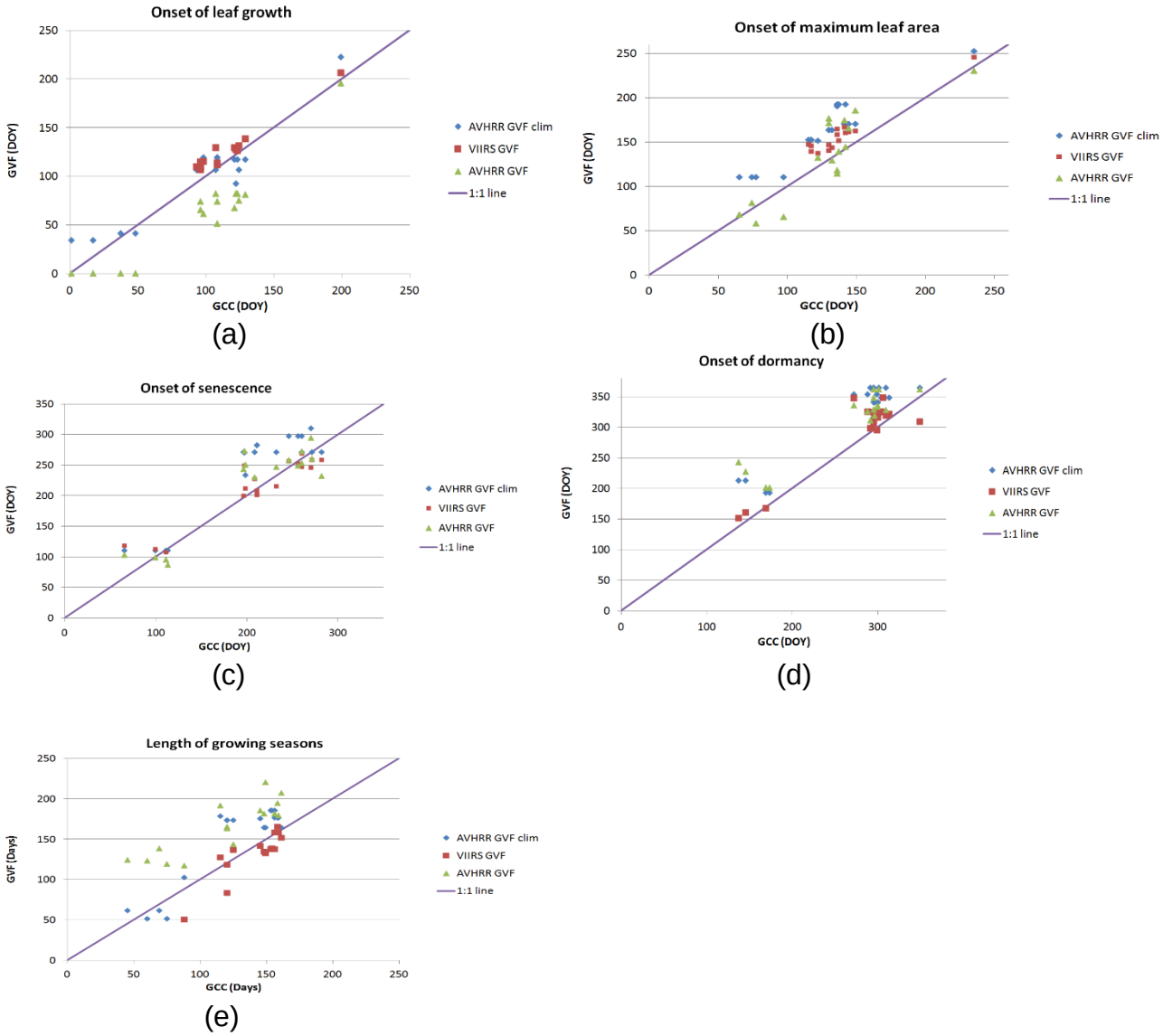

Figure 21. Scatter plots of Dates of onsets of leaf growth (a), maximum leaf area (b), senescence (c), dormance (d) and length of growing seasons (e) between GCC and GVF at the 10 PhenoCam sites.

Mean difference of the phenological dates between GCC and the GVF products were calculated and shown in Fig. 21. It is clearly shown that VIIRS GVF had the smallest difference with the GCC in all the phenological dates except for the dates of maximum leaf

area, which indicates that VIIRS GVF depicts the seasonal variation more accurately than the AVHRR GVF and the AVHRR GVF climatology.

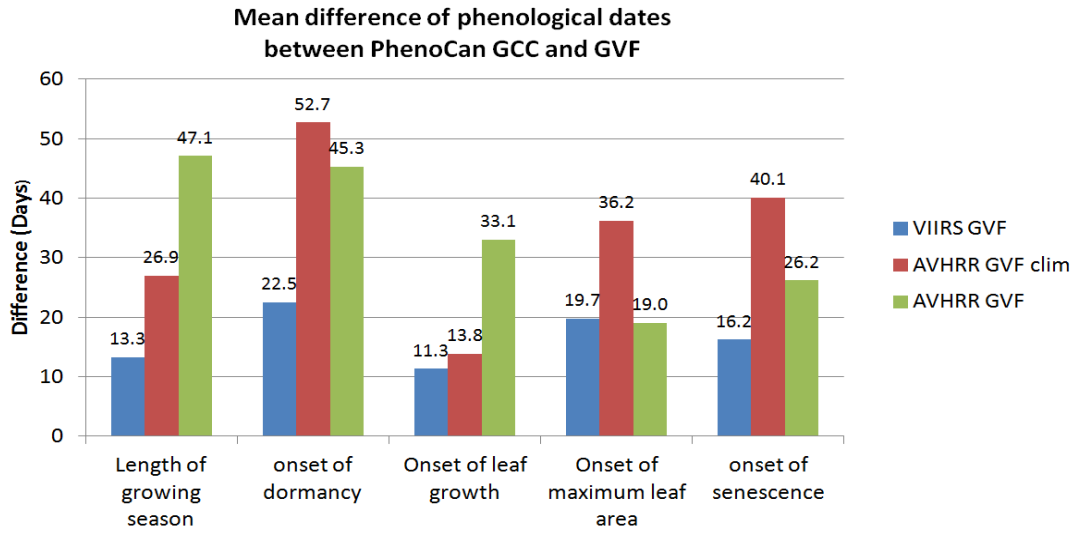

Figure 22. Mean difference of phenological dates between PhenoCam GCC and GVF.

4. ASSUMPTIONS AND LIMITATIONS

4.1 Assumptions

The assumption that was made in producing Green Vegetation Fraction product using GVF is:

- EVI change is slow and smooth from week to week. Abnormal jumps in EVI time series will be considered as noise and be removed.

4.2 Limitations

The GVF calculate green vegetation fraction for all areas including snow and high latitude areas. But for the high latitude area in the North Hemisphere in winter, there is no reliable data from the VIIRS sensor onboard the SNPP satellite due to the lack of sunlight or extremely high solar zenith angle (>80°). For pixels in this region, GVF is filled by the VIIRS

monthly GVF climatology. Abrupt GVF change could be possible on the boundary of the gap-filled areas.

5. LIST OF REFERENCES

Baret, F., J. G. P. W., Clevers, and M. D. Steven (1995). The robustness of canopy gap fraction estimations from red and near-infrared reflectances: a comparison of approaches. *Remote Sensing of Environment*, 54, 141-151.

Cabral, A., M. J. P. De Vasconcelos, J. M. C. Pereira, É. Bartholomé, and P. Mayaux (2003). Multi-temporal compositing approaches for SPOT-4 VEGETATION. *International Journal of Remote sensing*, 24, 3343-3350.

Cao C., DeLuccia F., Xiong X., Wolfe R., and Weng F. Weng (2013). Early On-orbit Performance of the Visible Infrared Imaging Radiometer Suite (VIIRS) onboard the Suomi National Polar-orbiting Partnership (S-NPP) Satellite*. IEEE Transactions on Geoscience and Remote Sensing* (DOI: 10.1109/TGRS.2013.2247768).

Carlson, T. N., and D. A. Ripley (1997). On the relation between NDVI, fractional vegetation cover, and leaf area index. *Remote Sensing of Environment*, 62, 241-252.

Carreiras, J. M. B., J. M. C. Pereira, Y. E. Shimabukuro, and D. Stroppiana (2003). Evaluation of compositing algorithms over the Brazilian Amazon using SPOT-4 VEGETATION data. *International Journal of Remote sensing*, 24, 3427-3440.

Cihlar, J., D. Manak, and M. D'Iorio (1994). Evaluation of compositing algorithms for AVHRR data over land. *IEEE Transactions on Geoscience and Remote Sensing*, 32, 427-437.

Deluccia, F., C. Cao (2011). VIIRS SDR Calibration/Validation Operations Concept (OPSCON) Document, JPSS program document, unpublished, 57.

Dymond, J. R., P.F. Stephens, and R. H. Wilde, (1992). Percentage vegetation cover of a degrading rangeland from SPOT. *International Journal of Remote sensing*, 13 (11), 1999-2007.

Friedl M. A., D. K. McIver, J. C. F. Hodges, X. Y. Zhang, D. Muchoney, A. H. Strahler, C.E. Woodcock, S. Gopal, A. Schneider, A. Cooper, A. Baccini, F. Gao, C. Schaaf (2002). Global land cover mapping from MODIS: algorithms and early results. *Remote Sensing of Environment*, 83, 287-302.

Gorry, A., (1990). "General least-squares smoothing and differentiation by the convolution (Savitzky–Golay) method". *Analytical Chemistry* **62** (6): 570–573.

Goward, S., B. Markham, and D. Dye (1991). Normalized difference vegetation index measurements from the advanced very high resolution radiometer. *Remote Sensing of Environment*, 35, 257−277.

Gutman, G. (1991). Vegetation indices from AVHRR: an update and future prospects. *Remote Sensing of Environment*, 35, 121-136.

Gutman, G., and A. Ignatov (1998). The derivation of the green vegetation fraction from NOAA/AVHRR data for use in numerical weather prediction models. *Int. J. Remote Sensing* 19**,** 1533-1543.

Holben, B. (1986). Characteristics of maximum-value composite images from temporal AVHRR data. *International Journal of Remote Sensing*, 7, 1417−1434.

Houborg, R., H. Soegaard, and E. Boegh (2007). Combining vegetation index and model inversion methods for the extraction of key vegetation biophysical parameters using Terra and Aqua MODIS reflectance data. *Remote Sensing of Environment*, 106, 39-58.

Huete, A. R. (1988). A soil-adjusted vegetation index (SAVI). *Remote Sensing of Environment,* 25, 295-309.

Huete, A. R., G. Hua, J. Qi, A. Chehbouni, and W. J. D. van Leeuwn (1992). Normalization of multidirectional red and NIR reflectances with the SAVI. *Remote Sensing of Environment*, 41, 143-154.

Huete, A. R., K. Didan, T. Miura, E. P. Rodriguez, X. Gao, and L. G. Ferreira (2002). Overview of the radiometric and biophysical performance of the MODIS vegetation indices. *Remote Sensing of Environment*, 83, 195-213.

Huete, A. R., K. Didan, Y. E. Shimabukuro, P. Ratana, C. R. Saleska, L. R. Hutyra, W. Yang, R. R. Nemani, and R. Myneni, (2006). Amazon rainforests green-up with sunlight in dry season. *Geophysical Research letters*, 33, L06405, dio:10.1029/2005GL025583.

Jeremy, I. F., F. M. John, A. V. Matthew, (2006). Green leaf phenology at Landsat resolution: scaling from the field to the satellite. *Remote Sensing of Environment*, 100, 265-279.

Jiang, L., F. N. Kogan, W. Guo, J. D. Tarpley, K. E. Mitchell, M. B. Ek, Y. Tian, W. Zheng, C., Z. Zou, and B. H. Ramsay (2010). Real-time weekly global green vegetation fraction derived from advanced very high resolution radiometer based NOAA operational global vegetation index (GVI) system. *J. Geophys. Res.,* 115, D11114, doi:10.1029/2009JD013204.

Jiang, Z,. A.R. Huete, K. Didan, T. Miura (2008). Development of a two-band enhanced vegetation index without a blue band. *Remote Sensing of Environment*, 112, 3833–3845.

Jiang, Z., A. R. Huete, J. Chen, Y. Chen, J. Li, G. Yan, and X. Zhang (2006). Analysis of NDVI and scaled difference vegetation index retrievals of vegetation fraction. *Remote Sensing of Environment*, 101, 366-378.

Jiang, Z., M. Vargas, and I. Csiszar (2014). Using the soil-adjusted vegetation index in compositing to reduce the bias in view angle directions. *ISPRS Journal of Photogrammetry and Remote Sensing*, submitted.

Kaufman, Y. J., and D. Tanré (1992). Atmospherically resistant vegetation index (ARVI) for EOS-MODIS. *IEEE Transactions on Geoscience and Remote Sensing*, 30, 261-270.

Kogan, F. N. (1990). Remote sensing of weather impacts on vegetation in non-homogeneous areas. *International Journal of Remote sensing*, 11 (8), 1405-1419.

Kogan, F. N., M. Vargas, H. Ding, and W. Guo (2011). Vegetation Health Products (VHP) algorithm theoretical basis document, version 1.1. NOAA/NESDIS/STAR.

Kustas, W. P., T. J. Schmugge, K. S. Humes, T. H. Jackson, R. Parry, M. A. Weltz, and M. S. Moran (1993). Relationships between evaporative fraction and remotely sensed vegetation index and microwave brightness temperature for semiarid rangelands. *Journal of Applied Meteorology*, 32, 1781-1790.

Leprieur, C., Y. H. Kerr, S. Mastorchio, and J. C. Meunier (2000). Monitoring vegetation cover across semi-arid regions: comparison of remote observations from various scales. *Int. J. Remote Sensing*, 21, 281-300.

Liu, H., and A. R. Huete (1995). A feedback based modification of the NDVI to minimize canopy background and atmospheric noise. *IEEE Transactions on Geoscience and Remote Sensing*, 33, 457-465.

Ormsby, J. P., B. J. Choudhury, and M. Owe (1987). Vegetation spatial variability and its effect on vegetation indices. *International Journal of Remote sensing*, 8, 1301-1306.

Phulpin, T., J. Noilhan, and M. Stoll (1990). Parameters estimates of a soil vegetation model using AVHRR data. Proceedings of the 4th AVHRR data users meeting, Rothenburg, Germany, 5-8 Sept. 1989. EUMETSAT, Darmstadt, EUM P 06, 125-129.

Purevdorj, T., R. Tateishi, T. Ishiyama, and Y. Honda (1998). Relationships between percent vegetation cover and vegetation indices. *International Journal of Remote sensing*, 19, 3519-3535.

Rahman, A. F., D. A. Sims, V. D. Cordova, and B. Z. El-Masri (2005). Potential of MODIS EVI and surface temperature for directly estimating per-pixel ecosystem C fluxes. *Geophysical Research Letters*, 32, L19404, doi:10.1029/2005GL024127.

Savitzky, A., Golay, M.J.E. (1964). "Smoothing and Differentiation of Data by Simplified Least Squares Procedures". *Analytical Chemistry* **36** (8): 1627–1639.

Sims, D. A., A. F. Rahman, E. F. Vermote, and Z. Jiang (2011). Seasonal and inter-annual variation in view angel effects on MODIS vegetation indices at three forest sites. *Remote Sensing of Environment,* 115, 3112-3120.

Sims, D. A., A. F. Rahman, V. D. Cordova, B. Z. El-Masri, D. D. Baldocchi, L. B. Flanagan, A. H. Goldstein, D. Y. Hollinger, L. Misson, R. K. Monson, W. C. Oechel, H. P. Schmid, S. C. Wofsy, and L. Xu (2006). On the use of MODIS EVI to assess gross primary productivity of North American ecosystems. *Journal of Geophysical Research*, 111, G04015, doi:10.1029/2006JG000162.

Stoms, D. M., M. J. Bueno, and F. W. Davis (1997). Viewing geometry of AVHRR image composites derived using multiple criteria. *Photogrammetric Engineering & Remote Sensing,* 63, 681-689.

Sullivan, J. (1993). Explanation of the filter that is presently used on NDVI weekly time series data to smooth out unrepresentative fluctuations from week to week. NOAA technical memorandum, January 14.

van Leeuwen, W. J. D., A. R. Huete, and T. W. Laing (1999). MODIS vegetation index compositing approach: a prototype with AVHRR data. *Remote Sensing of Environment,* 69, 264-280.

Wittich, K-P., and O. Hansing (1995). Area-averaged vegetative cover fraction estimated from satellite data. *International Journal of Biometeorology*, 38, 209-215.

Xiao, X., D. Hollinger, J. Aber, M. Goltz, E. A. Davidson, Q. Zhang, and B. Moore (2004). Satellite-based modeling of gross primary production in an evergreen needleleaf forest. *Remote Sensing of Environment*, 89, 519-534.

Zhang, X., A. F. Mark, B. S. Crystal, H. S. Alan, C. F. H. John, F. Gao, C. R. Bradley and A. Huete. (2003). *Remote Sensing of Environment*, 84, 471-475.

END OF DOCUMENT